

Flutter in Functionally Graded Conical Shell under Follower Force

Rupsagar Chatterjee¹, Sudib Kumar Mishra²

1 - Associate Engineer, Airbus Group India Private Limited, Bangalore, India

2 - Professor, Department of Civil Engineering, Indian Institute of Technology Kanpur, UP, India

ABSTRACT: Truncated conical shells are essential components of rocket booster nozzles and thrust vector control (TVC) systems for the propulsion of multi-stage launch vehicles. The TVCs assist the ascent of launch vehicles by directing the resultant thrust from the boosters, acting as a follower force that might trigger instability. Previous studies on instability are mostly limited to cylindrical shell geometry. This study analyses a truncated conical shell under a follower force of constant magnitude, considering thickness-wise gradation of elastic properties employed for thermal management. The governing equations are derived following Hamilton's principle, considering first-order shear deformation and, solved using finite element method, approximating the circumferential displacements by harmonic functions. Clamped and free boundaries are assumed at the small and large ends. The influence of mass and stiffness proportional damping is considered. Although strong flutter appears as the dominant instability mode, instances of erratic weak instabilities are also observed for undamped and lightly damped cases. Long shells with small semi-vertex angles are noted to be less susceptible to weak instability but exhibit much lower flutter load. The non-dimensional flutter load attains saturation in long shells with small semi-vertex angle beyond a thickness parameter. The critical load decreases monotonically for increasing slenderness, except for small semi-vertex angles and thickness parameters greater than 0.1, for which it increases shortly before reduction. The flutter loads for undamped and lightly damped cases are highly sensitive to changing geometry. Although damping enhances stability, its effect gets saturated. The flutter loads are presented for varying non-dimensional parameters, characterizing the shell geometry and material properties.

Keywords: Functionally Graded Material, Truncated Conical Shell, Follower Force, Flutter, Finite Element Method

Correspondence to: Sudib Kumar Mishra; **E-mail:** smishra@iitk.ac.in

1. Introduction

Shells are widely used in engineering because of their efficient load-carrying behavior, high strength-to-weight ratio, and ability to contain space by their geometry. Shells find wide applications as storage structures, containment for nuclear power plants, domes, pressure vessels, aircraft propulsion systems, fuselages, rockets, missiles, ships, and submarines. Many biological lifeforms like plants, animals, and human organs (eyes, skull, bones, and joints) are inherently shell structures.

Functionally graded materials (FGMs) are an advanced class of inhomogeneous composite materials. But unlike conventional composites, the mechanical, thermal, and chemical properties of FGMs can vary smoothly across thickness. Because of this, no material interface appears, although the resulting FGM inherits its constituents' properties. The gradual change of properties alleviates several difficulties associated with conventional materials. It improves the bond strength by eliminating any stress singularity that can otherwise be present in composites. Moreover, FGMs can reduce residual stresses in high thermal gradient environments due to the gradually changing thermal expansion coefficient. FGMs have found widespread applications as super heat-resistant refractory materials in spacecraft, nuclear reactors, high-efficiency energy conversion materials, biomaterials, and optical and electronic components (Koizumi and Niino 1995; Koizumi 1997). Functionally graded shells have gained prominence in recent years as a viable structural material for launch vehicles, owing to the feasibility of creating thermal barriers in structures exposed to high-temperature gradients.

Depending on the functional gradation of material properties, FGMs can be of three types: power-law (P), exponential (E), and sigmoid (S). PFGM and EFGM are the most commonly used descriptions of FGM where the constituent materials vary as per power-law and exponential functions, respectively (Chi and Chung 2006). However, in both these FGM, stress concentration occurs at one of the interfaces where the material composition varies rapidly. To eliminate this, a sigmoid variation can be introduced, where the volume fraction is defined using two power-law functions. SFGMs have been shown to reduce the stress intensity factor and arrest crack growth in cracked specimens (Chi and Chung 2003).

Over the past century, researchers have put forward various theories of shells. These include significant contributions by Sanders (1959), Novozhilov (1964), Vlasov (1964), and Flügge (1966), among many others. These works are commonly referred to as classical shell theories, in which the Kirchhoff-Love hypothesis with thin shell assumptions approximates

the displacement fields. Leissa (1993) comprehensively studied various thin shell theories applied to different shell geometries. Contrary to the theories of thin shells, thick shell theories consider the effect of transverse shear deformations and rotary inertia. The rotations of the normal to the surface are considered in addition to the displacement components.

Early works on truncated conical shells mainly dealt with free vibration analysis using different analytical and numerical techniques by adopting isotropic or laminated composite materials. These include works by Irie et al. (1984), Kayran and Vinson (1990), Tong (1993), Shu (1996), Liew et al. (2005) and many others. Recent studies in advanced numerical simulations of plates and shells incorporate alternate choices of materials, including but not limited to functionally graded (FG) or carbon nanotube (CNT) reinforced nanocomposites, owing to their widespread applications. Bhangale et al. (2006) studied the linear thermoelastic buckling and free vibration characteristics of FG first-order shear deformable truncated conical shells subjected to high-temperature environment using finite element approach. Tornabene et al. (2009) presented the free vibration analysis of FG conical and cylindrical shells and annular plates employing moderately thick shell assumptions. Malekzadeh et al. (2012) studied the three-dimensional free vibration of FGM truncated conical shells subjected to thermal environment using the differential quadrature method (DQM). Nejati et al. (2017) presented a parametric study of free vibration of CNT-reinforced FG truncated conical shell using generalized differential quadrature (GDQ) and third-order shear deformation theory (TSDT). Zghal et al. (2018a) analyzed the free vibration of CNT-reinforced FG composite shells. Song et al. (2019) investigated the free vibration characteristics of truncated conical shells with non-classical boundary conditions having elastic constraints and added mass. Fares et al. (2021) showed the free vibration analysis of CNT-reinforced multilayered FG truncated conical shell with mixed mode formulation. Li et al. (2021) analyzed the free vibration of porous metal foam truncated conical shell under elastic boundary conditions considering first-order shear deformation theory (FSDT) and different porosity distributions. Zghal et al. (2021) determined the thermal free vibration characteristics of FGM plates and shells using an improved FSDT shell model. Avramov et al. (2022) studied the transient response of FG-CNT-reinforced conical shell with ring-stiffener using higher-order shear deformation theory (HSDT) and the Rayleigh-Ritz method. Wang et al. (2022) presented the free vibration analysis of a spinning FG spherical-cylindrical-conical shell with arbitrary boundary conditions in a thermal environment. Vescovini and Fantuzzi (2023) analyzed the free vibration of conical shells using the Ritz method with arbitrary boundary conditions.

Several studies investigating the stability characteristics of FGM shells and plates can also be found in the literature. Sofiyev (2012) studied the nonlinear vibration of FG truncated conical shell with large deformation theory and von Karman-Donnell type kinematic nonlinearity. Zghal et al. (2018b) showed the buckling analysis of power-law based FG and FG-CNT-reinforced plates and curved panels employing higher order shell model in nonlinear finite element framework. Trabelsi et al. (2018; 2019) investigated the thermal buckling and post-buckling of FG plates and cylindrical shells using modified FSDT. Trabelsi et al. (2020) also investigated the thermal buckling and post-buckling response of FG plates and shells using a geometrically nonlinear Kirchhoff shell model. Allahkarami et al. (2020) presented the dynamic buckling of a bi-directional functionally graded (BD-FG) truncated conical shell on an elastic foundation with FSDT. The governing equations are derived using Hamilton's principle and solved by the GDQ method. Zarei et al. (2020) studied the global buckling behavior of laminated sandwich conical shells with lattice cores for different design parameters employing FSDT and the Galerkin method. Fu et al. (2021) analytically determined the dynamic instability of FG sandwich conical shells under periodic axial and lateral loads using Mathieu-Hill equations and the GDQ method. Zghal et al. (2022) analyzed the post-buckling behavior of FG-CNT-reinforced composites. Zghal and Dammak (2021) studied the vibration characteristics of porous imperfect FGM plates and shells with modified FSDT. Using Galerkin's method, Huang et al. (2023) performed vibration and buckling analysis of porous SFGM truncated conical shell. Hasan et al. (2023) investigated the buckling and post-buckling behavior of laminated graphene-enhanced composite (GEC) truncated conical shells subjected to torsion and thermal environment.

Lately, several studies have been conducted on flutter instability of functionally graded plates and shells in supersonic airflow. Ibrahim et al. (2008) presented the flutter and post-buckling behavior of functionally graded rectangular plates using nonlinear finite element analysis considering thermal effects and aerodynamic pressure, using thin plate assumption. In another work, Ibrahim et al. (2009) also studied the flutter phenomenon in thin rectangular FGM plates using nonlinear finite element method under the combined effect of supersonic airflow, thermal, and random acoustic loads. Mahmoudkhani et al. (2010) determined the aeroelastic stability boundaries of simply supported FGM conical shells subjected to supersonic flow under a thermal environment. Sabri and Lakis (2013) proposed a hybrid finite element formulation based on Sanders' thin shell theory and finite element method to predict flutter in FGM cylindrical shells under supersonic airflow. Su et al. (2019) developed a unified approach for the vibration and flutter analysis of elastically restrained

first-order shear deformable stiffened FGM plates. Wei et al. (2020) studied the flutter behavior of axially functionally graded (AFG) cylindrical shells. It was shown that such structures could have superior aeroelastic qualities with a judicious choice of parameters. Sun et al. (2021) argued that the aeroelastic stability of systems could be improved against flutter by adding lumped masses, which may be an effective design methodology for the AFG panels. Muc and Flis (2021) presented free vibration and flutter behavior for porous functionally graded rectangular plates using analytical and Rayleigh-Ritz methods. Zhou et al. (2021) showed the free vibration and flutter characteristics of graphene platelet (GPL) reinforced porous FGM cylindrical panels. AminYazdi (2021) performed a flutter analysis of FG-CNT-reinforced double-curved shells with geometric imperfections. Avramov and Uspensky (2022) investigated the geometrically nonlinear flutter instability of a sandwich truncated conical shell with honeycomb core under supersonic flow. Houshang et al. (2022) analyzed the supersonic flutter of a sandwich truncated conical shell with a magneto-rheological (MR) core. Banijamali and Jafari (2023) recently studied the vibration characteristics and critical speeds of rotating FG conical shells stiffened with anisogrid lattice structure.

In the context of shells with follower force, Park and Kim (2000) studied the dynamic instability of a free-free cylindrical shell with FSDT. Torki et al. (2014a) performed a dynamic instability analysis of cantilever FGM cylindrical shells subjected to follower force. In another study, Torki et al. (2014b) investigated the flutter of cantilever FGM cylindrical shells considering uniformly distributed and linearly increasing follower forces.

FGM truncated conical shells are one of the essential structural components in the propulsion system of launch vehicles. In present-day multi-stage launch vehicles, they find extensive use as rocket booster nozzles and thrust vector control (TVC) systems. After the propellant combustion in booster engines, the nozzle extension at the rear end of the launch vehicle discharges the exhaust to generate the required thrust for lift-off and subsequent flight of the vehicle. During this operation, high pressure acts on the nozzle, causing elastic deformations in its body. These deformations change the direction of the generated thrust from the boosters. Of course, the TVCs assist in sophisticated maneuvering in the flight path during the ascent of the launch vehicle by appropriately directing the resultant thrust from the boosters. Nevertheless, a follower force acts on the nozzle.

It is evident from the ongoing discussion that though the behavior of space launching structures has been idealized as cylindrical shells and beams under follower force in previous investigations, a lacuna exists in the study of stability characteristics of truncated conical

shells subjected to follower force. The present study aims to address this research gap. This study presents the stability behavior of FG truncated conical shells subjected to follower force of constant magnitude. The governing equations of the first-order shear deformable shell is derived using Hamilton's principle and solved the using finite element method, approximating the circumferential displacements by harmonic functions. The convergence and validity of the proposed model are checked; then, some parametric studies are conducted. The study accommodates varying geometry of the shells by adjusting the semi-vertex angle, slant height, radius, and thickness. Different characteristics of the material properties (namely, the damping, functional gradation exponent, and so on) for the shell are included in the analysis to study their influences on the stability against flutter. The remainder of the article is organized as follows. *Section 2* illustrates the adopted shell model with the governing equations and explains the solution methodology. *Section 3* discusses the mesh sensitivity of the proposed finite element model and validates it with the existing literature. The dynamic instability characteristics of the FGM truncated conical shell are presented along with an overview of free vibration behavior. The results from the parametric studies are presented here. *Section 4* summarizes the article with concluding remarks.

2. Formulation of the governing equations

The geometry of a truncated conical shell is shown in *Figure 1*. In this figure, α refers to the semi-vertex angle of the complete cone. The coordinate system is taken in a way, such that the s coordinate axis runs along a meridian starting from the apex of the cone to the larger base and acts as a generator of the surface. The angular coordinate θ runs circumferentially at any section from a reference meridian. The direction normal to both s and θ is taken to be the z direction and is taken positive outward from the shell middle surface. The shell is assumed to have constant thickness h . The s coordinates of the smaller and larger ends of the shell are taken as s_1 and s_2 respectively, and respective radii are denoted by r_1 and r_2 . The symbol l is the slanted height of the frustum. The radius r of the mid-surface ($z = 0$) at any distance s from the apex of the cone is then given as,

$$r(s) = s \sin \alpha \quad (1)$$

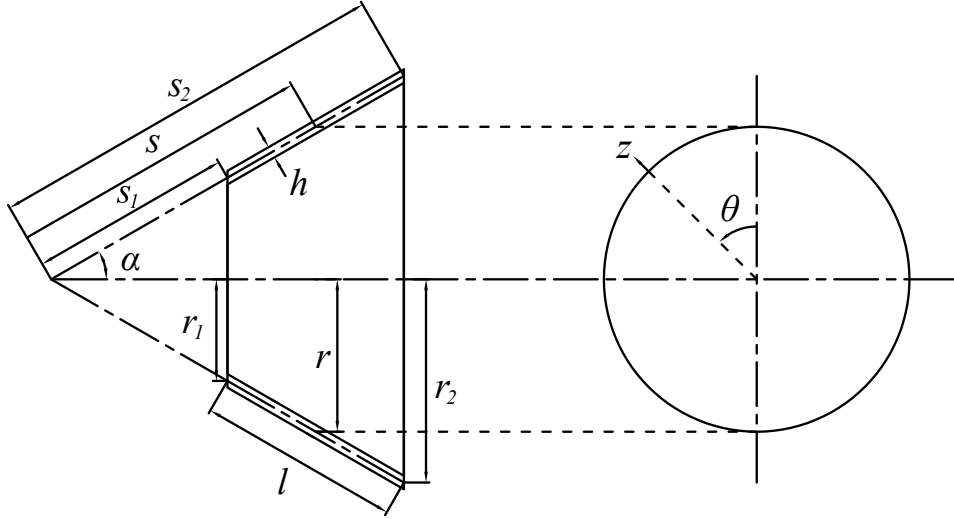


Figure 1 Geometry of a truncated conical shell along with the reference coordinate system

For studying the dynamic stability, the smaller end of the conical shell is assumed to be clamped whereas the larger end is kept free. The larger end is subjected to a uniformly distributed follower force of constant intensity P , shown in *Figure 2*. This force is assumed to be acting along the mid-surface of the shell and remains tangential to the meridian at all points on the edge at any configuration of the shell. Thus, the direction of the follower force at any two diametrically opposite points on the free edge would not be parallel due to the conical shape of the shell, which is unlike the case of a cylindrical shells, for which the meridians are parallel to the surface generator.

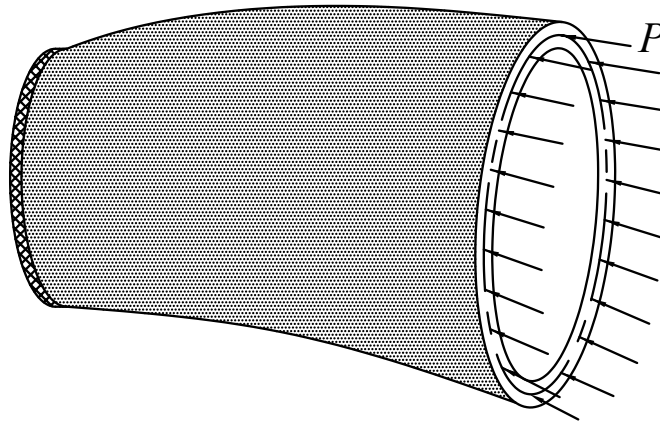


Figure 2 Schematic representation of a truncated conical shell with clamped small end and free large end subjected to uniformly distributed follower force in deformed geometry along the mid-surface of the larger edge

The density, Young's modulus and Poisson's ratio for the FG shell at any depth z from the mid-surface are denoted by ρ , E and ν respectively. The Poisson's ratio for the FGM is reasonably assumed to be constant to avoid complexity (Reddy 2000). However, the density and Young's modulus vary continuously across the thickness of the shell. As such,

these quantities for the homogeneous constituent of the FGM are added with subscripts i and o (i.e. ρ_i , E_i , ρ_o and E_o) to represent the properties at the inner and outer shell surfaces, respectively. In this study, two FGM models are considered for the truncated conical shell, namely, power-law type FGM (PFGM) and the exponential type FGM (EFGM) (Chi and Chung 2006).

The material properties vary as a power-law function of the volume fraction of the constituents in PFGM. Depending on the surface of choice, from where the volume fraction is controlled, alternative formulations can be found in the literature (Tornabene et al. 2009). In this work, the volume fraction of the inner surface constituent at any depth z is taken as,

$$V_i(z) = \left(\frac{1}{2} - \frac{z}{h} \right)^\eta \quad (2)$$

Here, $z/h = -0.5$ corresponds to the inner surface of the truncated conical shell. The total volume fraction of the inner and outer surface constituents at any depth within the shell is always unity. That is, $V_i(z) + V_o(z) = 1$, where, V_o is the volume fraction of the outer surface constituent. Using the rule of mixtures, the density and Young's modulus at any point in the PFGM becomes,

$$\rho(z) = \rho_i V_i(z) + \rho_o V_o(z) = \rho_i \left(\frac{1}{2} - \frac{z}{h} \right)^\eta + \rho_o \left\{ 1 - \left(\frac{1}{2} - \frac{z}{h} \right)^\eta \right\} \quad (3.1)$$

$$E(z) = E_i V_i(z) + E_o V_o(z) = E_i \left(\frac{1}{2} - \frac{z}{h} \right)^\eta + E_o \left\{ 1 - \left(\frac{1}{2} - \frac{z}{h} \right)^\eta \right\} \quad (3.2)$$

where the volume fraction index η ($0 \leq \eta < \infty$) determines the variation profile of the constituent materials. For $\eta = 0$, the PFGM shell is completely composed of the inner surface material whereas, for $\eta \rightarrow \infty$, it is entirely composed of the outer surface material. Naturally, these cases represent the special case of a shell with homogeneous material. In EFGM, the material properties between the two surfaces of a truncated conical shell vary exponentially as follows (Chi and Chung 2006),

$$\rho(z) = \rho_o e^{\left(\frac{1}{2} - \frac{z}{h} \right) \ln \left(\frac{\rho_i}{\rho_o} \right)} \quad (4.1) \quad E(z) = E_o e^{\left(\frac{1}{2} - \frac{z}{h} \right) \ln \left(\frac{E_i}{E_o} \right)} \quad (4.2)$$

A moderately thick shell is considered in the present work and therefore the Reissner-Mindlin first-order shear deformation theory (FSDT) is used for analysis. Based on the

assumptions of the first-order shear deformation theory, the displacement components $(\bar{u}, \bar{v}, \bar{w})$ at any point in the shell having coordinates (s, θ, z) at time t is written as,

$$\bar{u}(s, \theta, z, t) = u(s, \theta, t) + z\phi(s, \theta, t) \quad (5.1)$$

$$\bar{v}(s, \theta, z, t) = v(s, \theta, t) + z\psi(s, \theta, t) \quad (5.2)$$

$$\bar{w}(s, \theta, z, t) = w(s, \theta, t) \quad (5.3)$$

where u , v and w represent the displacement components of the shell middle surface in the s , θ and z directions respectively. The quantities ϕ and ψ denote the rotations of the normal to the middle surface with respect to s and θ directions, respectively. No shear correction factor is assumed in the analysis. Using equations (5.1) to (5.3), the strains at any point then becomes (Soedel 2004),

$$\boldsymbol{\varepsilon} = \boldsymbol{\Xi} \boldsymbol{A} \quad (6)$$

where the strain vector $\boldsymbol{\varepsilon} = [\varepsilon_{ss} \quad \varepsilon_{\theta\theta} \quad \varepsilon_{s\theta} \quad \varepsilon_{sz} \quad \varepsilon_{\theta z}]^T$ and the generalized displacement vector $\boldsymbol{A} = [u \quad v \quad w \quad \phi \quad \psi]^T$. The kinematic operator $\boldsymbol{\Xi}$ is as per equation (A.1). Assuming linearly elastic, isotropic material property, the stress-strain ($\boldsymbol{\sigma}$ - $\boldsymbol{\varepsilon}$) relation can be written as,

$$\boldsymbol{\sigma} = \boldsymbol{D} \boldsymbol{\varepsilon} \quad (7)$$

where the stress vector $\boldsymbol{\sigma} = [\sigma_{ss} \quad \sigma_{\theta\theta} \quad \sigma_{s\theta} \quad \sigma_{sz} \quad \sigma_{\theta z}]^T$. The constitutive matrix \boldsymbol{D} is given in equation (A.2).

Applying the Hamilton's principle, the equation of motion for the truncated conical shell subjected to follower force can be written as,

$$\int_{t_1}^{t_2} (\delta T - \delta U - \delta V + \delta W_{nc}) dt = 0 \quad (8)$$

where δT , δU , δV represent the variations of the kinetic energy, strain energy and potential energy due to the conservative part of the follower force, whereas δW_{nc} represents the virtual work done by the non-conservative part of the follower force, respectively (Kim and Kim 2000; Park and Kim 2000; Simites and Hodges 2006). Individual terms of the integrand are obtained as,

$$\delta T = \int_0^{2\pi} \int_{s_1}^{s_2} \int_{-\frac{h}{2}}^{\frac{h}{2}} \rho \left\{ \dot{u} \delta \dot{u} + \dot{v} \delta \dot{v} + \dot{w} \delta \dot{w} + z^2 (\dot{\phi} \delta \dot{\phi} + \dot{\psi} \delta \dot{\psi}) \right\} (s \sin \alpha + z) dz ds d\theta \quad (9.1)$$

$$+ z \left(\dot{u} \delta \dot{\phi} + \dot{\phi} \delta \dot{u} + \dot{v} \delta \dot{\psi} + \dot{\psi} \delta \dot{v} \right)$$

$$\delta U = \int_0^{2\pi} \int_{s_1}^{s_2} \int_{-\frac{h}{2}}^{\frac{h}{2}} \boldsymbol{\varepsilon}^T \mathbf{D} \delta \boldsymbol{\varepsilon} (s \sin \alpha + z) dz ds d\theta \quad (9.2)$$

$$\delta V = P \int_0^{2\pi} \int_{s_1}^{s_2} \left(\frac{\partial w}{\partial s} \frac{\partial \delta w}{\partial s} + \frac{\partial v}{\partial s} \frac{\partial \delta v}{\partial s} \right) s \sin \alpha ds d\theta \quad (9.3)$$

$$\delta W_{nc} = P \int_0^{2\pi} \left[\left(\delta w \frac{\partial w}{\partial s} + \delta v \frac{\partial v}{\partial s} \right) s \sin \alpha \right]_{s=s_2} d\theta \quad (9.4)$$

where $(\dot{})$ denotes differentiation with respect to time. The solution of the generalized displacements can be assumed in the following form (Bhangale et al. 2006),

$$u(s, \theta, t) = \sum_{n=0}^{\infty} e^{\Lambda t} \bar{U}(s) \cos n\theta \quad (10.1) \quad v(s, \theta, t) = \sum_{n=0}^{\infty} e^{\Lambda t} \bar{V}(s) \sin n\theta \quad (10.2)$$

$$w(s, \theta, t) = \sum_{n=0}^{\infty} e^{\Lambda t} \bar{W}(s) \cos n\theta \quad (10.3) \quad \phi(s, \theta, t) = \sum_{n=0}^{\infty} e^{\Lambda t} \bar{\Phi}(s) \cos n\theta \quad (10.4)$$

$$\psi(s, \theta, t) = \sum_{n=0}^{\infty} e^{\Lambda t} \bar{\Psi}(s) \sin n\theta \quad (10.5)$$

where, \bar{U} , \bar{V} , \bar{W} , $\bar{\Phi}$ and $\bar{\Psi}$ are the shape functions of the respective displacement fields along the s direction and n denotes the circumferential wave number.

Hereafter, the finite element method is preferably used to solve the governing equations. A three-noded Lagrangian element is adopted for discretization of the truncated conical shell along the s coordinate. It may be noted that the approximation along the θ coordinate leads to a ring element in the circumferential direction of the shell. Following the above, the generalized displacement vector is given as,

$$\bar{\Delta} = \sum_{n=0}^{\infty} e^{\Lambda t} \mathbf{N}^{(n)} \bar{\Delta} \quad (11)$$

where $\mathbf{N}^{(n)}$ is the shape function matrix in the n -th circumferential mode, which is a function of s and θ ; the symbol $\bar{\Delta}$ is the generalized nodal displacement vector at the shell mid-surface in the discretized geometry. Using equation (11), the expression for strain in equation (6) becomes,

$$\boldsymbol{\varepsilon} = \sum_{n=0}^{\infty} e^{\Lambda t} \boldsymbol{\Xi} \mathbf{N}^{(n)} \bar{\Delta} = \sum_{n=0}^{\infty} e^{\Lambda t} \mathbf{B}^{(n)} \bar{\Delta} \quad (12)$$

It can be seen from equations (9.1) to (9.4) that the shape functions are mutually orthogonal with respect to the circumferential bases. This is true for shells with axisymmetric geometry and boundary conditions (Leissa 1993). Since the equations hold true for any arbitrary

circumferential mode, they can be solved separately for each n . Thus, the summations and the superscripts in equations (11) and (12) can be conveniently dropped without loss of generality. Taking N_{elem} as the total number of elements in the discretized geometry, \mathbf{d} as the unrestrained nodal DOFs, and substituting equations (11) and (12) into equation (8) with correct assembly of the element matrices and imposing boundary conditions, one obtains,

$$(\Lambda^2 \mathbf{M} + \mathbf{K} - P\mathbf{C} + P\mathcal{N})\mathbf{d} = \mathbf{0} \quad (13)$$

The system mass (\mathbf{M}) and stiffness ($\mathbf{K}, \mathbf{C}, \mathcal{N}$) matrices are obtained by evaluating the integrals analytically using commercial symbolic algebra software *Maple*. It can be shown that \mathbf{M} , \mathbf{K} and \mathbf{C} will yield symmetric matrices while \mathcal{N} will be non-symmetric matrix. Further, it can be found that the matrices \mathbf{M} , \mathbf{C} and \mathcal{N} are independent of the circumferential wave number n while \mathbf{K} is not. From equation (13) taking $\mathbf{Q} = \mathcal{N} - \mathbf{C}$, the eigenvalue problem can be written as,

$$\det(\Lambda^2 \mathbf{M} + \mathbf{K} + P\mathbf{Q}) = 0 \quad (14)$$

Damping has been introduced in the structure as mass and stiffness proportional damping (Jung and Han 2014). Assuming identical damping ratio (ζ) for the first two vibration modes, the damping matrix is taken as (Chopra 2012),

$$\mathbf{C} = \gamma_1 \mathbf{M} + \gamma_2 \mathbf{K} \quad (15)$$

where γ_1 , γ_2 are related to the first two undamped natural frequencies (Ω_1, Ω_2) as per equation (A.3). Incorporating the effect of damping, equation (13) gets modified as,

$$(\Lambda^2 \mathbf{M} + \Lambda \mathbf{C} + \mathbf{K} + P\mathbf{Q})\mathbf{d} = \mathbf{0} \quad (16)$$

The above equation can be transformed into standard linear eigenvalue problem $\mathbf{A}\mathbf{q} = \Lambda\mathbf{q}$ (Langthjem and Sugiyama 2000) and the eigenvalues are determined from,

$$\det(\mathbf{A} - \Lambda \mathbf{I}) = 0 \quad (17)$$

where,

$$\mathbf{A} = \begin{bmatrix} \mathbf{0} & \mathbf{I} \\ -\mathbf{M}^{-1}(P\mathbf{Q} + \mathbf{K}) & -\mathbf{M}^{-1}\mathbf{C} \end{bmatrix} \quad (18.1)$$

$$\mathbf{q} = \begin{bmatrix} \mathbf{d} \\ \Lambda \mathbf{d} \end{bmatrix} \quad (18.2)$$

In the foregoing discussion, $\mathbf{0}$ represents a null matrix or vector while \mathbf{I} represents an identity matrix of appropriate dimension. The eigenvalues Λ can be written as,

$$\Lambda = \Theta \pm i\Omega \text{ with } \Omega \geq 0 \quad (19)$$

Depending upon the values of Θ and Ω , four distinct cases may arise, as given in *Table 1*.

Table 1

Classification of the eigenvalue solution

Type of motion	Nature of eigen solution
Harmonic motion with constant amplitude	$\Theta = 0, \Omega > 0$
Harmonic motion with decreasing amplitude (Damped vibration)	$\Theta < 0, \Omega > 0$
Harmonic motion with increasing amplitude (Flutter instability)	$\Theta > 0, \Omega > 0$
Divergence instability	$\Theta > 0, \Omega = 0$

In the absence of damping and follower force, free vibration of the system is characterized with harmonic motion of constant amplitude, depending on the initial conditions. In case of damped system, the free vibration response is harmonic with decreasing amplitude. With the addition of follower force, the system undergoes flutter or divergence type of instability for certain critical value of the force depending upon the nature of the eigenvalue. The cyclic frequency of the system is given as, $f = \Omega / 2\pi$

The eigenvalue problems in equations (14) and (17) can be written in non-dimensional form by introducing the following parameters,

$$\rho_r = \frac{\rho_i}{\rho_o} \quad (20.1)$$

$$E_r = \frac{E_i}{E_o} \quad (20.2)$$

$$\xi_1 = \frac{h}{r_2} \quad (20.3)$$

$$\xi_2 = \frac{l \sin \alpha}{r_2} \quad (20.4)$$

$$\beta = P \frac{(1 - \nu^2)}{E_o h} \quad (20.5)$$

$$\lambda = \Lambda r_2 \sqrt{\frac{(1 - \nu^2) \rho_o}{E_o}} \quad (20.6)$$

where, $\lambda = \mathcal{G} \pm i\omega$ with $\omega \geq 0$.

The lowest magnitude of the follower force, for which an instability occurs is the critical load (P_{cr}). The corresponding non-dimensional value is denoted as β_{cr} . A numerical scheme is adopted from Barsoum (1971) and modified to adaptively increment the load parameter to improve computational efficiency for determining the onset of instability and the respective critical load. The algorithm for the solution methodology is given in *Appendix B*.

3. Numerical illustration

A computer program is developed in commercial software *MATLAB* for the finite element analysis of free vibration and dynamic instability of truncated conical shell subjected to follower force. The vibration characteristics and critical load for instability are presented subsequently by adopting representative values of the pertinent parameters for the conical shell geometry, as adopted in aerospace applications. The boundary conditions are denoted by F , S , and C for the free, simply supported and clamped cases, respectively, at each end of the shell. The subscripts S and L refers to the smaller and larger ends of the shell, respectively. The presentation is made using the following sub-sections.

3.1. Convergence study

A convergence study is performed to determine the number of finite elements required to suitably represent the cases of homogeneous and FGM shells for different parameter values. For this, only the mass and elastic stiffness matrices are retained in equation (14) for the free vibration eigen analysis. The constituent material properties for the FGM are adopted from Tornabene et al. (2009) and Zhao and Liew (2011), as furnished in *Table 2*. The value of the Poisson's ratio is assumed to be constant as 0.3.

Table 2

Properties of homogeneous constituents

Material	Poisson's ratio	Young's modulus	Density
Metal (Aluminum)	0.3	70 GPa	2707 kg/m ³
Ceramic – 1 (Zirconia)	0.3	151 GPa	3000 kg/m ³
Ceramic – 2	0.3	168 GPa	5700 kg/m ³

The undamped natural frequencies of the first few modes are determined considering varying finite element discretization of the shell geometry. The convergence results of the five lowest non-dimensional frequencies are given in *Table 3* for a homogeneous shell for two boundary conditions (S_S-S_L and S_S-C_L) using the PFGM model with $\eta \rightarrow \infty$ assuming any constituent material. Similarly, the convergence results for the five lowest cyclic frequencies are also shown in *Table 4* for two volume fraction indices of a PFGM truncated conical shell with aluminum as the outer constituent and ceramic – 2 as the inner constituent materials as per *Table 2*. The case with $\eta \rightarrow \infty$ is numerically mimicked by adopting a large value of 10^{30} . The values in the brackets represent the corresponding circumferential and longitudinal mode numbers (n, m) .

The natural frequencies are observed to converge well for around 15 elements for both the homogeneous as well as FGM shells. Henceforth, both the free vibration and

dynamic instability analyses employ 20 elements to reasonably discretize the shell along its slanted length.

Table 3

Convergence of lowest non-dimensional undamped natural frequency (ω) of truncated conical shell with homogeneous material properties $\alpha = 45^\circ$, $\xi_1 = 0.01$, $\xi_2 = 0.5$

Support	Number of elements (N_{elem})				
	5	10	15	20	25
S_S-S_L	0.2275 (0,1)	0.2251 (0,1)	0.2240 (0,1)	0.2235 (0,1)	0.2233 (0,1)
S_S-C_L	0.3793 (6,1)	0.3744 (6,1)	0.3736 (6,1)	0.3734 (6,1)	0.3733 (6,1)

Table 4

Convergence of lowest undamped natural frequency (f in Hz) of truncated conical shell with PFGM model, F_S-C_L boundary, $E_i = 168$ GPa, $\rho_i = 5700$ kg/m³, $E_o = 70$ GPa, $\rho_o = 2707$ kg/m³, $\alpha = 40^\circ$, $\xi_1 = 0.0459$, $\xi_2 = 0.7705$, $r_2 = 2.178$ m

η	Number of elements (N_{elem})				
	5	10	15	20	25
1	206.09 (2,1)	204.99 (2,1)	204.85 (2,1)	204.81 (2,1)	204.80 (2,1)
50	199.92 (2,1)	198.86 (2,1)	198.74 (2,1)	198.70 (2,1)	198.69 (2,1)

3.2. Verification of results

The results from the free vibration analyses are verified against the ones reported in literature for the homogeneous and the PFGM truncated conical shells. The non-dimensional undamped free vibration frequencies of the first longitudinal mode ($m = 1$) for homogeneous truncated conical shell are obtained from the PFGM model by adopting $\eta \rightarrow \infty$ with any of the constituent materials. The results are compared with Irie et al. (1984), Shu (1996) and Liew et al. (2005) (for different boundary conditions) in *Table 5*. For higher circumferential modes, the frequencies obtained from the present analysis are lower than that from the literature due to inclusion of the effect of rotary inertia.

The C_S-F_L boundary condition is used in this work to determine the free vibration and stability characteristics under follower force. The non-dimensional natural frequencies with C_S-F_L boundary condition for different α and ξ_2 values are presented and compared with Irie et al. (1984) in *Table 6* for homogeneous material.

The first five natural frequencies for PFGM truncated conical shell with aluminum as outer constituent and ceramic – 2 as inner constituent are determined for different values of η with F_S-C_L support condition. These are shown in *Table 7* and compared with the results

reported by Tornabene et al. (2009). The values in brackets respectively denote the circumferential and longitudinal mode numbers.

Table 5

Non-dimensional undamped natural frequency (ω) of truncated conical shell with homogeneous material, $\alpha = 45^\circ$, $\xi_1 = 0.01$, $\xi_2 = 0.5$, $m = 1$, $N_{elem} = 20$

	Present	Irie et al. (1984)	Shu (1996)	Liew et al. (2005)	Present	Irie et al. (1984)	Shu (1996)	Liew et al. (2005)
n	S_S-S_L				S_S-C_L			
0	0.2235	0.2233	0.2233	0.2234	0.8699	0.8698	0.8700	0.8691
1	0.5462	0.5462	0.5463	0.5462	0.8117	0.8117	0.8118	0.8113
2	0.6309	0.6310	0.6310	0.6309	0.6613	0.6614	0.6613	0.6610
3	0.5062	0.5065	0.5062	0.5061	0.5247	0.5249	0.5246	0.5244
4	0.3941	0.3947	0.3942	0.3941	0.4319	0.4324	0.4319	0.4316
5	0.3337	0.3348	0.3340	0.3337	0.3825	0.3834	0.3826	0.3822
6	0.3233	0.3248	0.3239	0.3235	0.3734	0.3747	0.3737	0.3732
7	0.3505	0.3524	0.3514	0.3510	0.3980	0.3997	0.3987	0.3980
8	0.4012	0.4033	0.4023	0.4019	0.4469	0.4489	0.4479	0.4472
9	0.4660	0.4684	0.4676	0.4671	0.5120	0.5142	0.5133	0.5124

Table 6

Non-dimensional undamped natural frequency (ω) of truncated conical shell with homogeneous material, C_S-F_L boundary, $\xi_1 = 0.01$, $m = 1$, $N_{elem} = 20$

	Present	Irie et al.(1984)	Present	Irie et al. (1984)	Present	Irie et al. (1984)
n	$\xi_2 = 0.25, \alpha = 30^\circ$		$\xi_2 = 0.25, \alpha = 45^\circ$		$\xi_2 = 0.25, \alpha = 60^\circ$	
0	0.8311	0.8312	0.6857	0.6859	0.4965	0.4966
1	0.6767	0.6768	0.6220	0.6221	0.4671	0.4672
2	0.4831	0.4831	0.5038	0.5039	0.4057	0.4059
3	0.3551	0.3553	0.4040	0.4042	0.3477	0.3480
n	$\xi_2 = 0.75, \alpha = 30^\circ$		$\xi_2 = 0.75, \alpha = 45^\circ$		$\xi_2 = 0.75, \alpha = 60^\circ$	
0	0.2267	0.2266	0.3205	0.3205	0.3926	0.3926
1	0.1187	0.1182	0.1576	0.1574	0.1502	0.1500
2	0.0549	0.0549	0.0780	0.0779	0.0772	0.0771
3	0.0458	0.0469	0.0573	0.0579	0.0590	0.0593

It can be seen from *Table 7* that the frequencies in a particular mode are highest when a shell is composed entirely of ceramic material ($\eta = 0$) and becomes lowest for a homogeneous shell made up of aluminum ($\eta \rightarrow \infty$). This is because the effect of an increase in Young's modulus on the frequency in a ceramic shell is more pronounced than the effect of increased density when compared with the metallic shell, i.e., $E_r > \rho_r$.

The results in *Table 5*, *Table 6* and *Table 7* show that the natural frequencies obtained from the present analysis for homogeneous or FGM truncated conical shells are in good agreement with the ones in existing literature.

Table 7

Undamped cyclic natural frequency (f in Hz) of truncated conical shell with PFGM model, F_S - C_L boundary, $E_i = 168$ GPa, $\rho_i = 5700$ kg/m³, $E_o = 70$ GPa, $\rho_o = 2707$ kg/m³, $\alpha = 40^\circ$, $\xi_1 = 0.0459$, $\xi_2 = 0.7705$, $r_2 = 2.178$ m, $N_{elem} = 20$

	Present	Tornabene et al. (2009)	Present	Tornabene et al. (2009)
f (Hz)	$\eta = 0$ (Ceramic)		$\eta = 0.6$	
1	210.03 (2,1)	209.99	205.88 (2,1)	205.96
2	232.09 (3,1)	231.96	225.63 (3,1)	225.52
3	288.09 (4,1)	287.48	278.52 (4,1)	277.93
4	322.67 (1,1)	322.57	317.89 (1,1)	318.18
5	357.28 (2,2)	356.95	349.57 (2,2)	349.48
f (Hz)	$\eta = 1$		$\eta = 5$	
1	204.81 (2,1)	204.91	203.84 (2,1)	203.93
2	224.56 (3,1)	224.44	227.86 (3,1)	227.67
3	277.29 (4,1)	276.66	285.02 (4,1)	284.26
4	315.93 (1,1)	316.32	309.19 (1,1)	309.57
5	347.72 (2,2)	347.66	347.21 (2,2)	347.08
f (Hz)	$\eta = 20$		$\eta = 50$	
1	200.72 (2,1)	200.79	198.70 (2,1)	198.73
2	224.39 (3,1)	224.29	220.97 (3,1)	220.86
3	280.71 (4,1)	280.15	275.47 (4,1)	274.93
4	304.93 (1,1)	305.04	303.46 (1,1)	303.46
5	342.02 (2,2)	341.87	338.32 (2,2)	338.11
f (Hz)	$\eta = 100$		$\eta \rightarrow \infty$ (Metal)	
1	197.80 (2,1)	197.79	196.73 (2,1)	196.69
2	219.34 (3,1)	219.21	217.39 (3,1)	217.23
3	272.92 (4,1)	272.38	269.85 (4,1)	269.28
4	302.87 (1,1)	302.83	302.24 (1,1)	302.14
5	336.64 (2,2)	336.39	334.65 (2,2)	334.35

3.3. Free vibration characteristics

The free vibration characteristics of the truncated conical shells are briefly reviewed in this section with special emphasis on the natural frequencies. This is because these modes have important bearing or participation in dynamic instabilities in the form of flutter. Henceforth, the PFGM and EFGM truncated conical shells are assumed to be composed of aluminum and zirconia along the outer and inner surfaces respectively, along with C_S - F_L boundary condition. The relevant material properties are given in *Table 2*.

The choice of the constituent materials for the FGM is logical since, in the exit cones of launch vehicles, the inner lining of the conical surface is exposed to very high temperatures from the exhaust of the rocket engines. In such cases, ceramics like zirconia can be effectively used as a heat-resistant material. Additionally, aluminum can be employed as a lightweight material on the outer surface of the FGM. In order to simulate the boundaries of a rocket nozzle, the smaller end is taken as clamped, where it is typically welded or forged to the body of the launch vehicle. The larger end of the shell is kept free.

The thickness-wise variation of the density and Young's modulus for the PFGM and EFGM shells are shown in *Figure 3*. The plots of PFGM are as per equations (3.1) and (3.2), while those of EFGM are obtained from equations (4.1) and (4.2) respectively. For the PFGM model, the density and Young's modulus at any depth are dependent on the volume fraction index η . For EFGM, the variation between the two surfaces is almost linear for density, whereas the Young's modulus shows a slight nonlinear variation for the chosen materials. From the plots of *Figure 3*, the free vibration and stability behavior of the EFGM model is expected to be identical to that of the PFGM with $\eta = 1$.

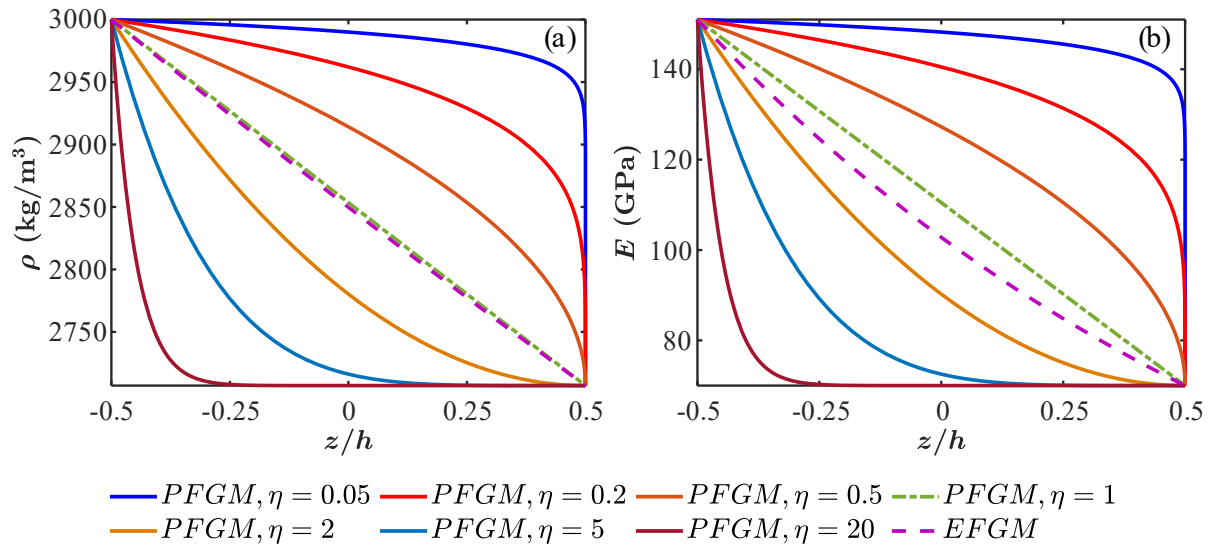


Figure 3 Comparison of density (ρ) and Young's modulus (E) across non-dimensional thickness (z/h) for EFGM and PFGM with varying volume fraction index (η) having aluminum and zirconia as outer and inner constituents respectively: (a) ρ vs z/h , (b) E vs z/h

Figure 4 presents the variations in the non-dimensional natural frequencies of the PFGM and EFGM shells for varying semi-vertex angle (α) with the first four circumferential modes and two damping ratios ($\zeta = 0, 0.2$) considering the first longitudinal

mode ($m=1$). The curves for intermediate damping ratios lie between these two curves. *Figure 5* shows the variation of the non-dimensional natural frequencies with semi-vertex angle for the first four longitudinal modes with the abovementioned damping ratios and the first circumferential mode ($n=0$). The damped natural frequencies do not differ significantly from the undamped frequencies even at 20 percent damping, which is an unrealistically large value of damping for FGM in practical cases and is assumed here only for illustration. This variation is almost negligible in case of the first two longitudinal modes. Further, it is also found that for lower α , the disparity between the damped and undamped frequencies is even smaller as compared to that at large α .

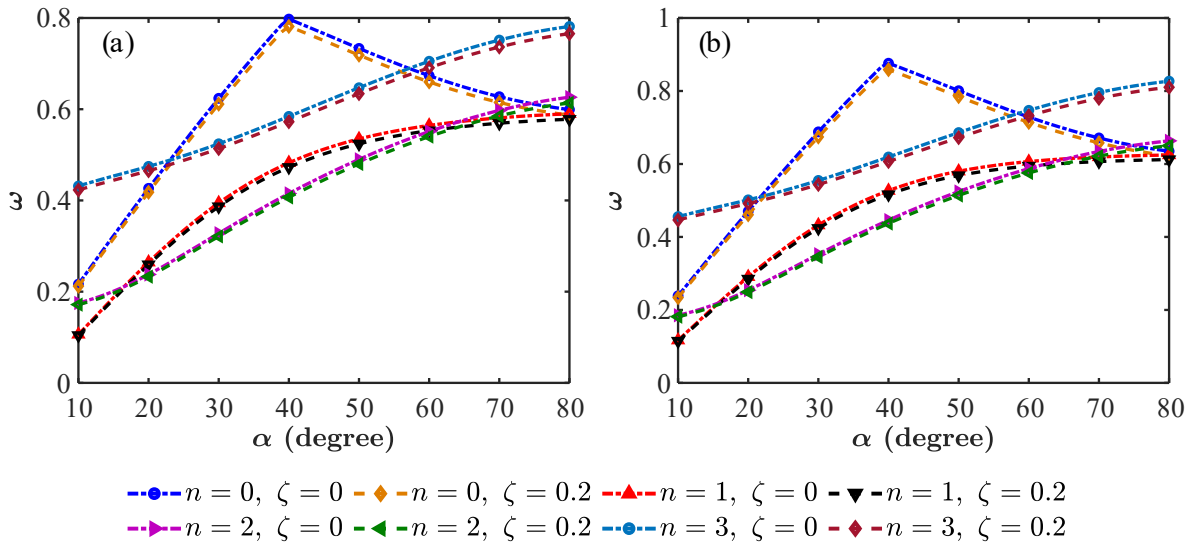


Figure 4 The effect of damping on non-dimensional frequency (ω) with varying semi-vertex angle (α), circumferential mode (n), damping ratio (ζ) for longitudinal mode (m)=1, thickness parameter (ξ_1)=0.15, slenderness parameter (ξ_2)=0.5: (a) PFGM with volume fraction index (η)=5, (b) EFGM

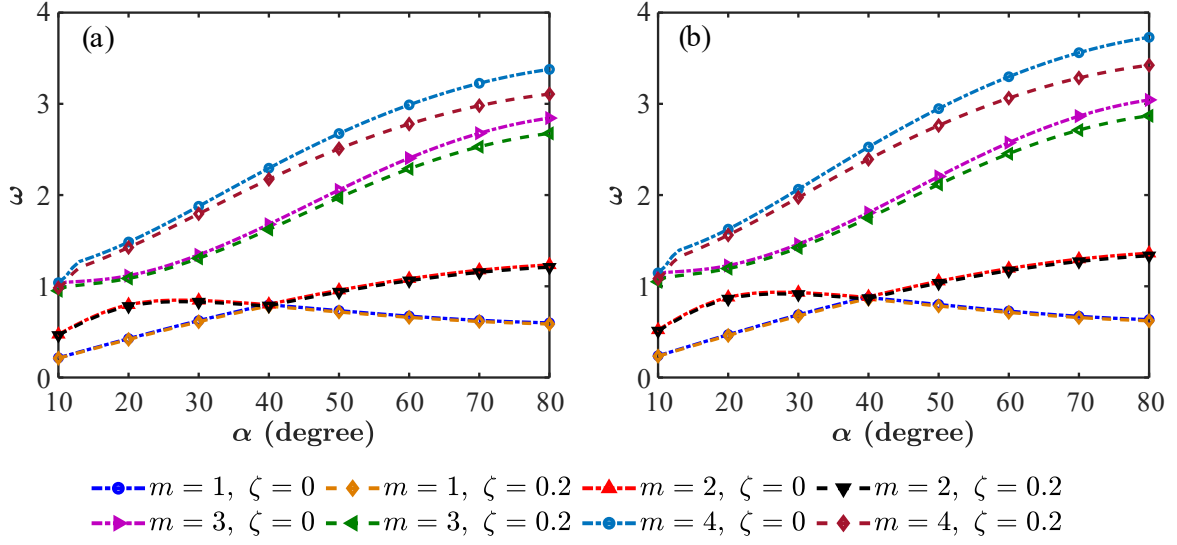


Figure 5 The effect of damping on non-dimensional frequency (ω) with varying semi-vertex angle (α), longitudinal mode (m), damping ratio (ζ) for circumferential mode (n)=0, thickness parameter (ξ_1)=0.15, slenderness parameter (ξ_2)=0.5: (a) PFGM with volume fraction index (η)=5, (b) EFGM

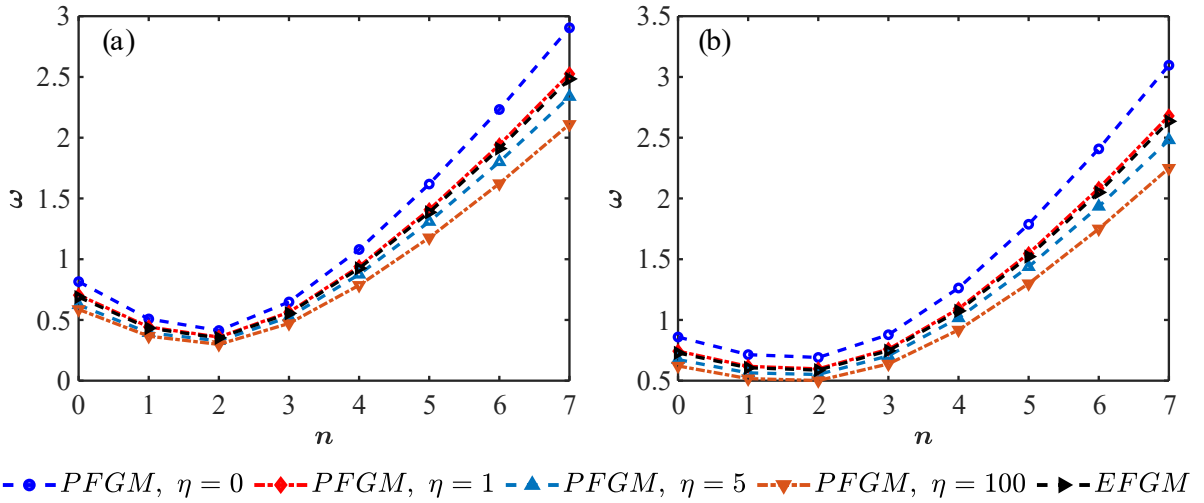


Figure 6 The non-dimensional frequency (ω) variation with circumferential mode (n) for EFGM and PFGM with varying volume fraction index (η), thickness parameter (ξ_1)=0.15, slenderness parameter (ξ_2)=0.5, damping ratio (ζ)=0, longitudinal mode (m)=1 and different semi-vertex angle (α): (a) $\alpha = 30^\circ$, (b) $\alpha = 60^\circ$

The variation of the first non-dimensional longitudinal frequency with different circumferential modes shows bath tub shapes in Figure 6. The natural frequencies decrease for increasing values of η with the chosen constituents due to the reason discussed in the

preceding section, i.e., $E_r > \rho_r$. The lowest frequencies occur at circumferential modes $n = 2, 2$ for $\alpha = 30^\circ, 60^\circ$ respectively. It is also interesting to note that the circumferential mode corresponding to the lowest frequency does not change with change in the η values. The mode shapes corresponding to the circumferential modes $n = 0$ (first) and $n = 1$ (second) are referred as the ‘breathing’ and ‘flexural’ modes, respectively.

3.4. Dynamic instability analysis

For the dynamic instability analysis of truncated conical shell, non-zero magnitude of the constant follower force is adopted while solving the eigenvalue problem in equations (14) and (17). For determination of the critical load, up to four circumferential ($n = 0, 1, 2, 3$) and four longitudinal modes ($m = 1, 2, 3, 4$) are considered for the undamped and damped cases of the shell. Analysis of the higher modes may require higher-order shear deformation theories, for improved accuracy in the estimation of the displacement fields. In the absence of damping, the dynamic instabilities obtained in the present analysis are strictly flutter-type. For this instability, two frequencies (ω) of the same circumferential mode (n) coalesce for a certain magnitude of the follower force. Presence of this critical follower force results in the real part of λ being positive ($\mathcal{G} > 0$). This causes the shell to experience motion with increasing amplitude under the constant follower force with progress in time.

For the damped structures, the system eigenvalues are twice in number as compared to the undamped case. In this case, flutter is not characterized by merging of two values of ω . Instead, only the real part of λ becomes greater than zero. Divergence is characterized by zero system frequency ($\omega = 0$) and real part of λ being positive ($\mathcal{G} > 0$) in both damped and undamped shells. The possible solutions for the governing equations are illustrated in *Table 1*. The algorithm described in *Appendix B* ensures the eigenvalues are initially sorted by the magnitude of λ to determine the longitudinal modes for any follower force. Both flutter and divergence type instability have been found to occur for the damped system. The flutter instability is seen to be critical for all parameter values as it occurs under a lower magnitude of the follower force.

Figure 7 shows the plots of the real and imaginary parts of the non-dimensional eigenvalue subjected to varying non-dimensional load in undamped shell with characteristic geometry and material parameters. It shows the coalescence of the third and fourth

longitudinal modes ($m=3,4$) accompanied by positive real part. The flutter load can be identified from these plots as 0.0289.

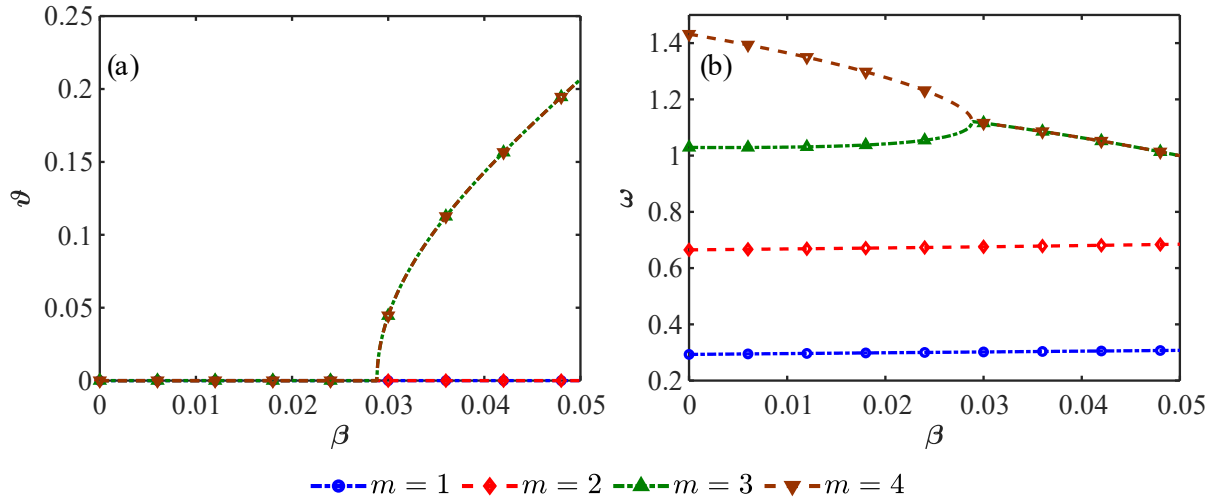


Figure 7 Flutter instability showing positive real (g) part and coalesced imaginary (ω) part of non-dimensional eigenvalue for different non-dimensional load (β), longitudinal mode (m) of PFGM with damping ratio (ζ)=0, circumferential mode (n)=0, volume fraction index (η)=10, semi-vertex angle (α)=30°, thickness parameter (ξ_1)=0.1, slenderness parameter (ξ_2)=0.7: (a) g vs β , (b) ω vs β

Weak flutter instabilities are observed for certain combination of the pertinent parameter values. The critical follower force value for weak flutter are considerably lower than the general trend of the flutter load in the parameter space. The weak flutter instabilities disappear on increasing follower force magnitude beyond a particular value, unlike strong flutter instability. Subsequent to weak flutter, a strong flutter is again observed at a higher magnitude of follower force, which does not go away with increasing value of the follower force. Instances of weak flutter and subsequent strong flutter are shown in *Figure 8* considering an undamped shell. The second and third longitudinal modes coalesce initially for a certain value of the follower force, indicating weak flutter. However, the coalesced eigenpath bifurcates subsequently into two distinct eigenpaths at a higher magnitude of the follower force. On further increasing the follower force, the first and second frequencies are seen to coalesce to give rise to a strong flutter instability.

The weak flutter instabilities are significantly suppressed in the presence of damping. At higher damping values, such weak instabilities get suppressed even more, and the plot of the critical load becomes a smooth curve in the parametric space. It can be attributed to the

fact that the stability of the structure enhances with increased damping as it helps in the dissipation of energy in the system through alternate path resulting in higher critical loads.

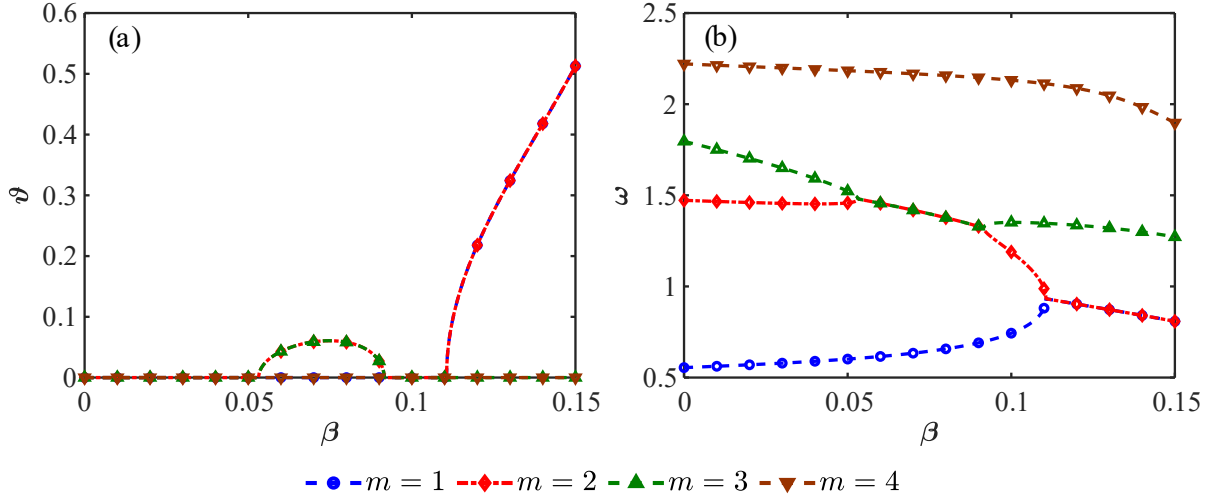


Figure 8 The variation of real (g) and imaginary (ω) part of non-dimensional eigenvalue with non-dimensional load (β) showing strong and weak flutter instabilities of PFGM with different longitudinal mode (m) for damping ratio (ζ) = 0, circumferential mode (n) = 1, volume fraction index (η) = 5, semi-vertex angle (α) = 30° , thickness parameter (ξ_1) = 0.16, slenderness parameter (ξ_2) = 0.4: (a) g vs β , (b) ω vs β

3.5. Influence of parametric variations on the flutter load

This section presents the parametric variations of the non-dimensional flutter load considering different geometric parameters, damping, and functional gradations of the FG truncated conical shell. The variation of the non-dimensional flutter load β_{cr} for different gradation index η are shown in *Figure 9* for changing ξ_2 , ξ_1 , α , ζ values. Common to all these plots is the reducing critical load with increasing metallic constituent, marked by higher gradient index (η). This trend can be attributed to the fact that the non-dimensional frequencies of the truncated conical shell decrease for higher volume fraction indices, previously demonstrated in *Figure 6*. Although, the maximum critical load is observed for ceramic shells, yet functional gradation is desirable to incorporate the lightweight metallic constituent in the shell. The results are presented hereafter for only two values of η ; namely $\eta=1$ and $\eta=5$. The former ($\eta=1$) gives a linear variation of the volume fraction in the FGM.

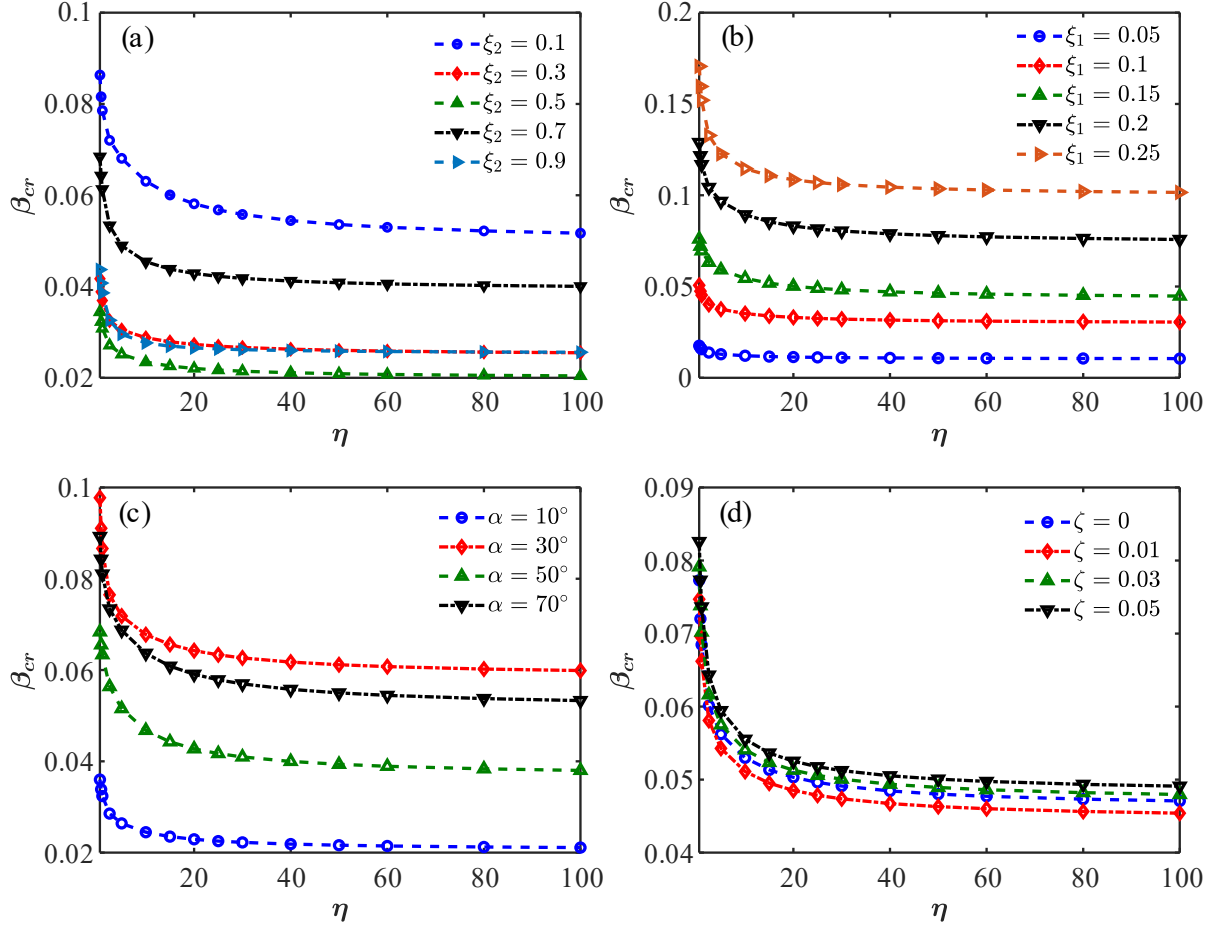


Figure 9 The dependence of non-dimensional critical load (β_{cr}) on volume fraction index (η) of PFGM for different slenderness parameter (ξ_2), thickness parameter (ξ_1), semi-vertex angle (α), damping ratio (ζ): (a) $\zeta = 0$, $\alpha = 10^\circ$, $\xi_1 = 0.15$, (b) $\zeta = 0$, $\alpha = 60^\circ$, $\xi_2 = 0.6$, (c) $\zeta = 0$, $\xi_1 = 0.15$, $\xi_2 = 0.6$, (d) $\alpha = 40^\circ$, $\xi_1 = 0.15$, $\xi_2 = 0.9$

Figure 10 presents the non-dimensional critical load for varying values of the thickness parameter (ξ_1). The trends are presented for varying level of damping ($\zeta = 0, 0.01, 0.03, 0.05$). The subplots (a-d) considers varying combination of (η , ξ_2 , α), listed therein. The critical load increases with higher damping ratios. However, the increase in the critical load beyond around three percent damping is negligible in most cases. As discussed previously, the sudden drops in the load parameter for low ζ values are due to the formation of weak flutter instabilities, which of course stabilizes for increased values of damping.

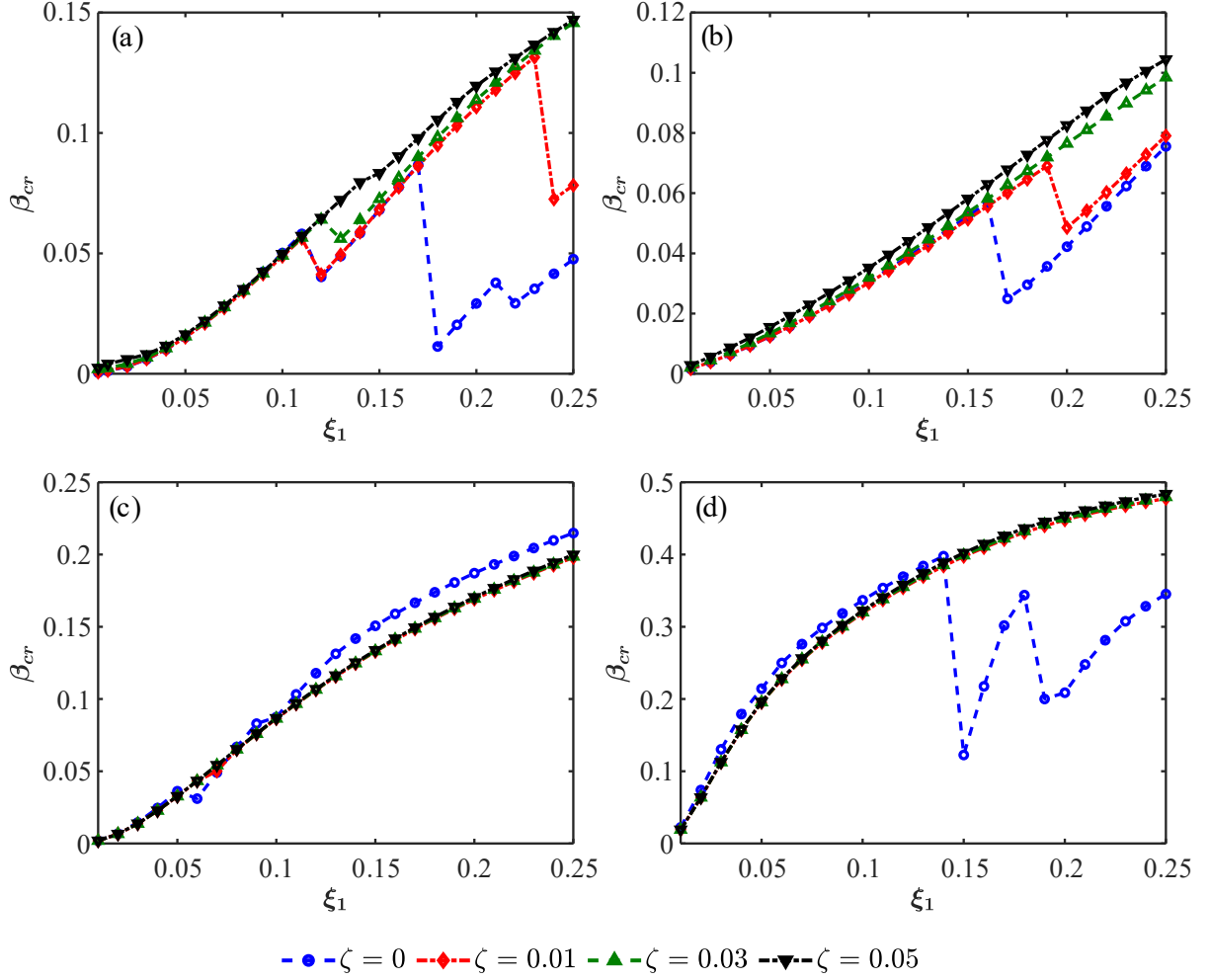


Figure 10 The effect of damping on non-dimensional critical load (β_{cr}) of PFGM with different thickness parameter (ξ_1), damping ratio (ζ), volume fraction index (η), slenderness parameter (ξ_2), semi-vertex angle (α): (a) $\eta = 5$, $\xi_2 = 0.1$, $\alpha = 10^\circ$, (b) $\eta = 5$, $\xi_2 = 0.7$, $\alpha = 30^\circ$, (c) $\eta = 5$, $\xi_2 = 0.3$, $\alpha = 60^\circ$, (d) $\eta = 1$, $\xi_2 = 0.1$, $\alpha = 80^\circ$

The curves for $\zeta = 0$ should ideally always be below the other ζ curves, but this is not observed for certain instances, like in *Figure 10-(c, d)*. Such anomalous behavior can be attributed to the fact that the present analysis includes only the first four longitudinal modes for the undamped case. Many more weak instabilities could be found, if higher longitudinal modes are included in the analysis. This would have caused the $\zeta = 0$ curve to always lie below the higher ζ curves. Subsequent results presented herein are shown by taking only zero and three percent damping in the first two modes, which is reasonable for all practical purposes.

The critical load corresponding to the identical circumferential wave numbers and identical coalescing longitudinal modes follows a smooth curve, as presented in *Figure 11*.

The isolated points indicate that they are not part of any of the plotted eigenmodes. The critical load curve in the parametric space (denoted by a solid line) is obtained by joining the lowest non-dimensional loads corresponding to each parameter value.

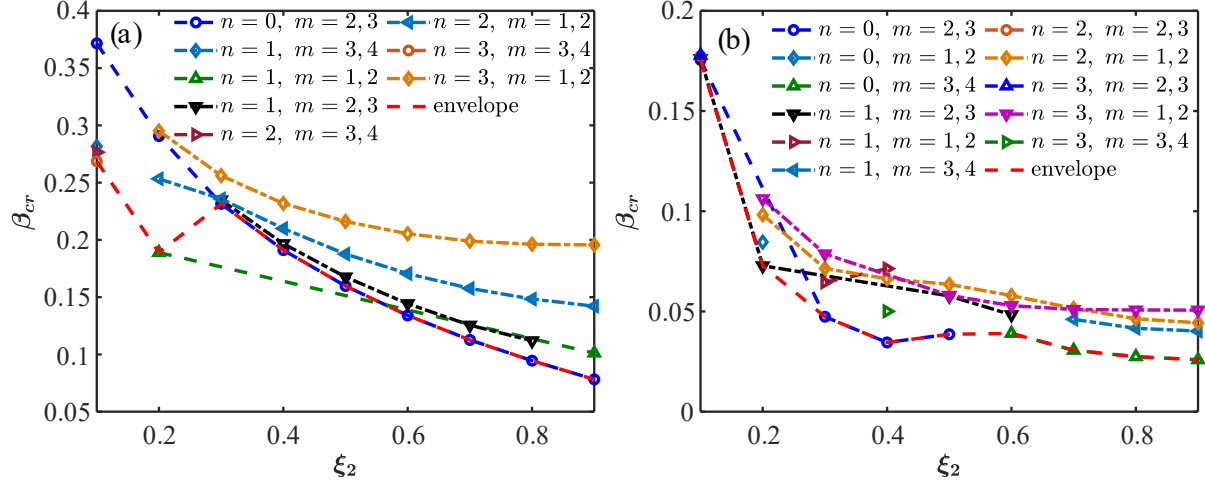


Figure 11 Curves of identical eigenmodes and envelope of non-dimensional critical load (β_{cr}) of PFGM with varying slenderness parameter (ξ_2), semi-vertex angle (α), thickness parameter (ξ_1) for volume fraction index (η)=5, damping ratio (ζ)=0: (a) $\alpha = 80^\circ$, $\xi_1 = 0.25$, (b) $\alpha = 30^\circ$, $\xi_1 = 0.1$

The plots of the non-dimensional critical load (β_{cr}) with varying thickness parameter (ξ_1) are shown in *Figure 12* and *Figure 13* for different slenderness parameters (ξ_2), damping ratios (ζ), semi-vertex angles (α) and volume fraction indices (η) of the PFGM. The number of drops in critical load due to weak instabilities reduces in *Figure 12*-(b) as compared to *Figure 12*-(a) due to the stabilizing effect of the increased damping. *Figure 12*-(b, d) and *Figure 13*-(a, b) show that the weak instabilities tend to lie in identical regions on the parametric space for different η . An increasing trend in the critical load with increasing thickness parameter (ξ_1) is seen, which is evident as thicker shells should exhibit instability under larger follower force, if other parameters remain identical. The critical loads are lower for shells with higher values of slenderness parameter (ξ_2) for any range of the semi-vertex angle. Increased ξ_2 keeping other parameters constant implies that the shell is longer and hence becomes more susceptible to instability. Moreover, weak instabilities are not that frequent for shells having large ξ_2 values. This is because such shells being longer are comparatively more unstable. Hence the onset of any instability is expected to grow and dominate as a strong flutter instability in the system.

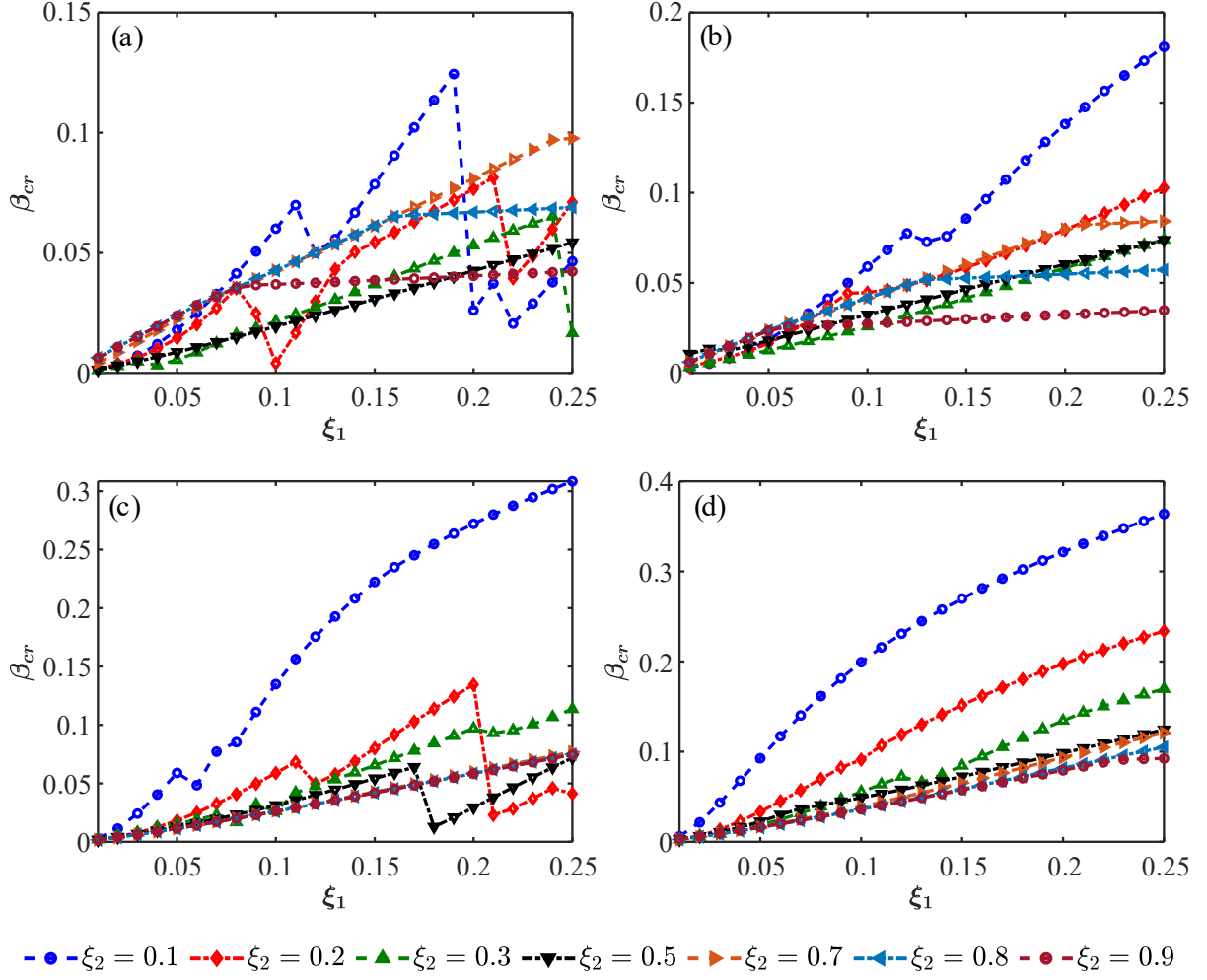


Figure 12 Non-dimensional critical load (β_{cr}) of PFGM for different thickness parameter (ξ_1), slenderness parameter (ξ_2), damping ratio (ζ), semi-vertex angle (α) with volume fraction index (η)=1: (a) $\zeta = 0, \alpha = 10^\circ$, (b) $\zeta = 0.03, \alpha = 10^\circ$, (c) $\zeta = 0, \alpha = 20^\circ$, (d) $\zeta = 0.03, \alpha = 30^\circ$

Roughly in the range of $0.7 \leq \xi_2 \leq 0.9$ and $\alpha \leq 40^\circ$, the critical load parameter (β_{cr}) attains saturation or varies negligibly beyond a certain ξ_1 . Although β_{cr} remains constant, it does not imply that the dimensional critical load will also be constant. This is because the dimensional load is proportional to the thickness of the shell, and it increases linearly due to increasing ξ_1 . Interestingly, a similar observation has also been reported in the case of a completely free cylindrical shell subjected to follower force by Park and Kim (2000). It follows from the present study that such a phenomenon of the constant non-dimensional critical load must also exist in the case of sufficiently long cylindrical shells under follower force with C_S - F_L boundary condition (Torki et al. 2014b). It is because a truncated conical

shell with small α and large ξ_2 values can be approximated as a long cylindrical shell in the limiting sense. Moreover, the parametric space shows a parabolic variation of β_{cr} with ξ_1 in *Figure 13* for increasing semi-vertex angles ($\alpha \geq 30^\circ$) and decreasing slenderness parameter (ξ_2) of the damped FG shell.

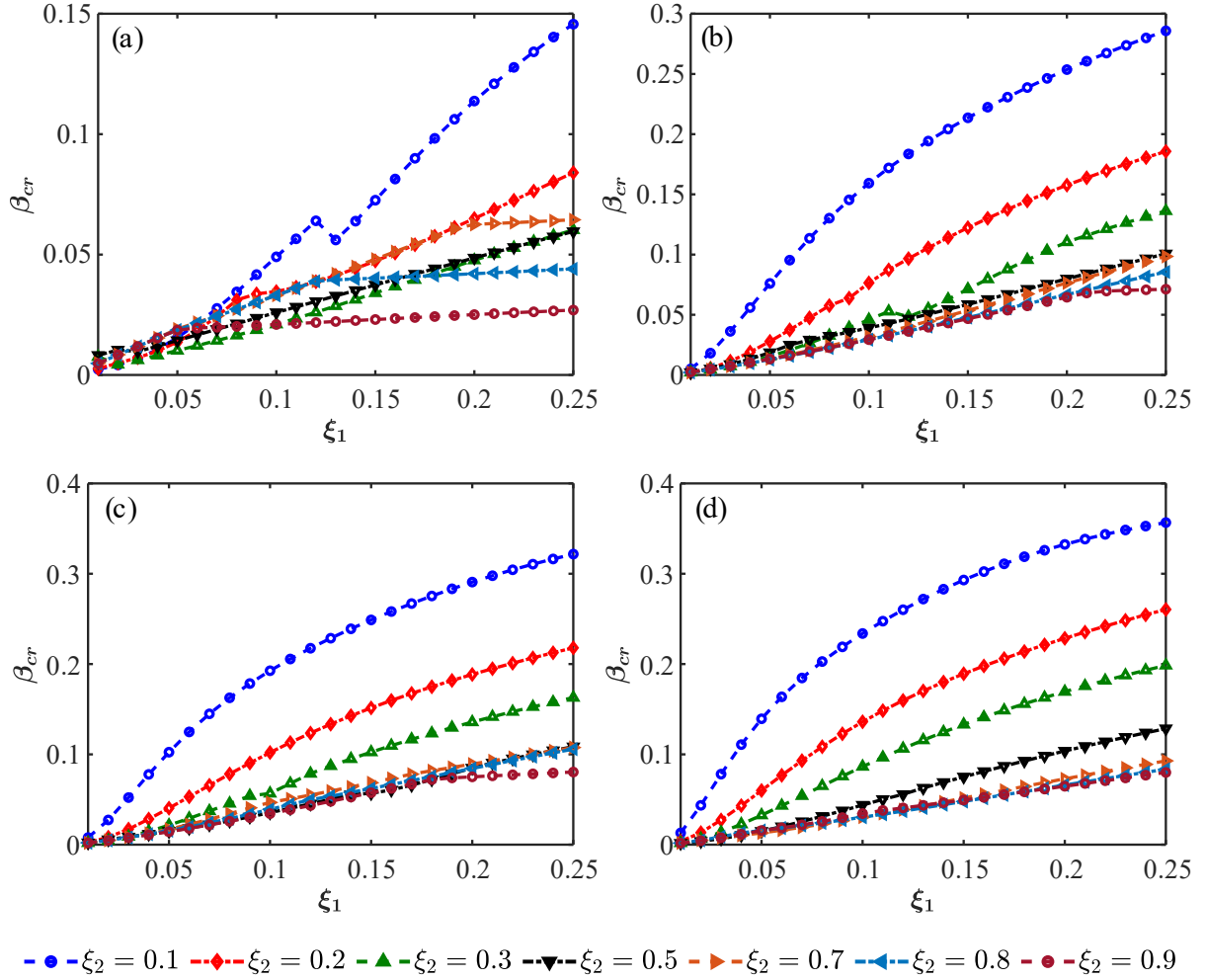


Figure 13 Non-dimensional critical load (β_{cr}) of PFGM with varying thickness parameter (ξ_1) for different slenderness parameter (ξ_2), semi-vertex angle (α), and volume fraction index (η) = 5, damping ratio (ζ) = 0.03: (a) $\alpha = 10^\circ$, (b) $\alpha = 30^\circ$, (c) $\alpha = 40^\circ$, (d) $\alpha = 60^\circ$

Comparison between *Figure 12-(a, c)* and *Figure 14* show that all parameters being identical, the critical loads in the EFGM model are close to that of the PFGM model with $\eta = 1$.

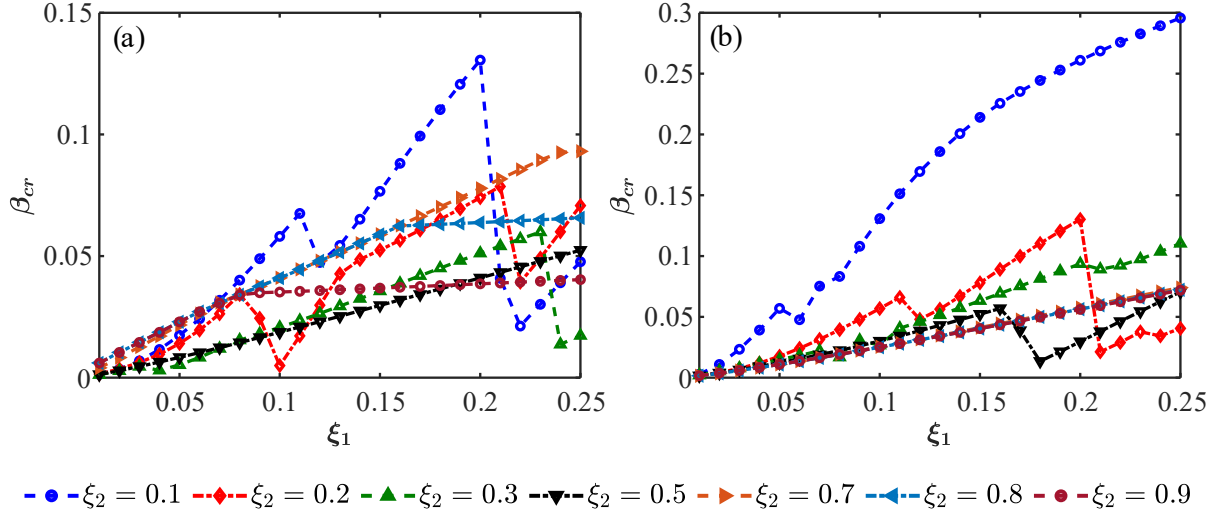


Figure 14 The variation of non-dimensional critical load (β_{cr}) with thickness parameter (ξ_1) of EFGM for varying slenderness parameter (ξ_2), damping ratio (ζ) = 0 and different semi-vertex angle (α): (a) $\alpha = 10^\circ$, (b) $\alpha = 20^\circ$

Figure 15 present the variation of β_{cr} with varying ξ_2 for different combination of the ($\alpha, \xi_1, \eta, \zeta$) values. For a semi-vertex angle (α) of the truncated conical shell less than 40° and thickness parameter (ξ_1) greater than 0.1, the critical flutter load (β_{cr}) first decreases up to a particular slenderness parameter (ξ_2) and then increases shortly before decreasing again. This reduction in the critical load after the rising part is because of a mode jump from a lower circumferential wave number to a higher mode, triggering the flutter. This is identical to the formation of an Arnold's tongue. These curves also merge for large ξ_2 values because the non-dimensional critical load attains constant value for changing ξ_1 as seen before. Keeping other parameters constant, the critical load is also found to increase with increasing semi-vertex angle of the conical shell. For other parametric values, the critical load decreases monotonically with increasing ξ_2 . In general, the non-dimensional critical load of the truncated conical shell reduces for a decrease in the semi-vertex angle, reduction in thickness, or an increase in the length of the shell.

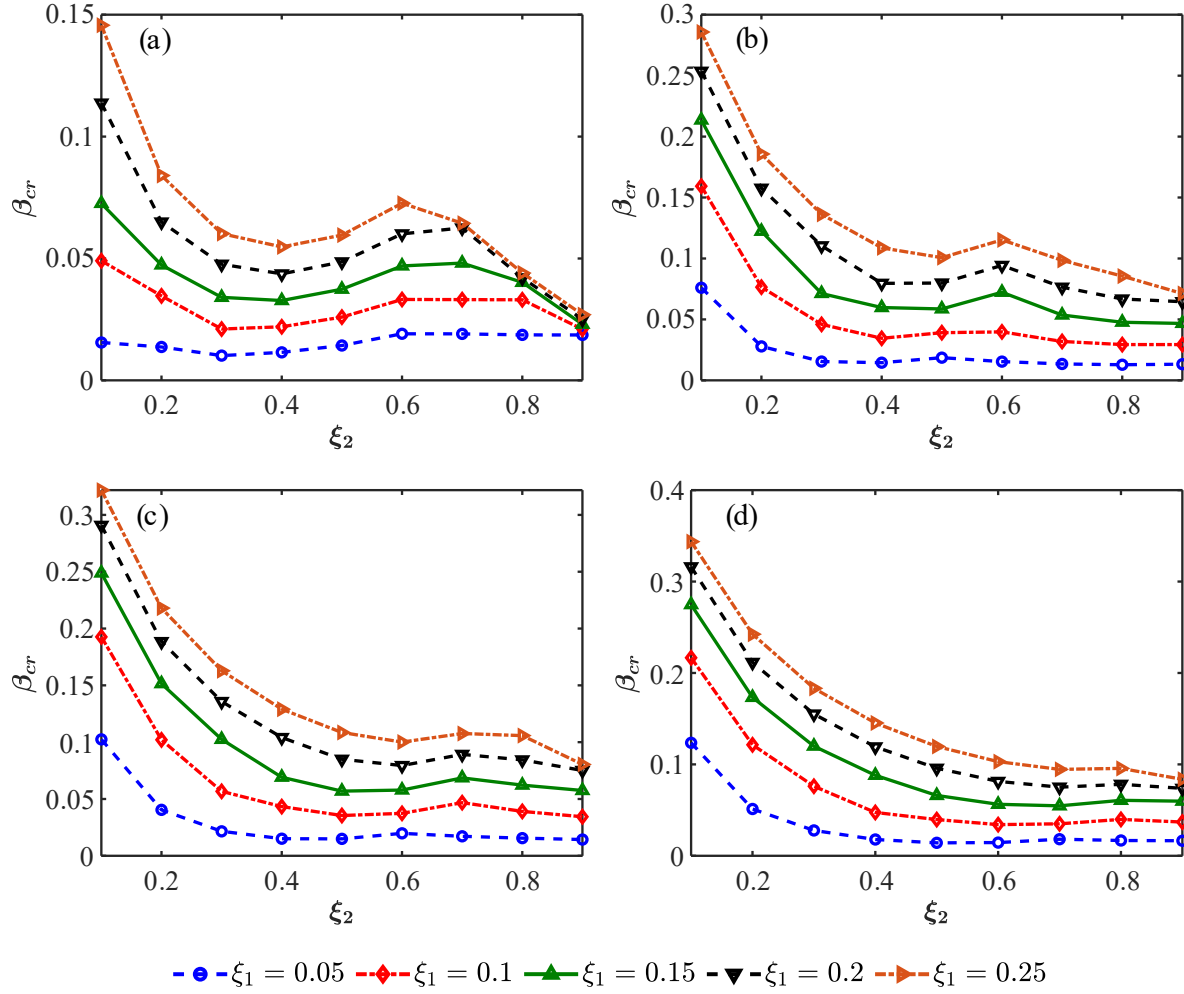


Figure 15 Non-dimensional critical load (β_{cr}) for varying slenderness parameter (ξ_2) of PFGM with different thickness parameter (ξ_1), different semi-vertex angle and volume fraction index (η)=5, damping ratio (ζ)=0.03 and (α): (a) $\alpha = 10^\circ$, (b) $\alpha = 30^\circ$, (c) $\alpha = 40^\circ$, (d) $\alpha = 50^\circ$

4. Summary and conclusions

The stability behavior of FG truncated conical shells under follower force is presented by adopting a simple yet efficient finite element formulation. The analyses explain the effects of the shell geometry and material properties on the critical flutter load, expressed in terms of several non-dimensional parameters involving the geometry and material properties. The FG truncated conical shell is assumed to be clamped at the smaller edge and free at the larger edge and is subjected to a uniformly distributed follower force at the free end. Power-law and exponential functional gradations across the shell thickness are considered. A three-noded Lagrangian element discretization is adopted along the meridian, whereas harmonic basis is employed along the circumference for approximating the displacement field. A mesh

convergence study is conducted to ascertain the suitable mesh size for discretization. The analysis is verified against the free vibration characteristics reported in earlier studies.

Mass and stiffness proportional damping is considered. The analysis under follower force reveals flutter-type instability in undamped shells, whereas both flutter and divergence instabilities occur for damped shells. The flutter happens for a lower magnitude of the follower force as compared to divergence. Many erratic weak instabilities are also observed for undamped and lightly damped shells, manifested as drastic drops in the load from the general trend of the critical flutter load in the parameter space. Long shells with small semi-vertex angles are relatively less susceptible to weak instabilities even though they exhibit a much lower critical load. It becomes imperative to perform instability analysis for undamped and lightly damped short truncated conical shells subjected to follower forces. The stability of the shell is sensitive to even a slight perturbation in its geometric properties. Structural damping enhances stability by increasing the magnitude of the critical load, but its effect beyond three percent damping is almost negligible.

For a given circumferential wave numbers, the locus of a pair of identical coalescing (longitudinal) modes results in smooth envelope curves. The lowest of all these critical loads gives the general variation of the critical load in the parameter space. The critical flutter load for the PFGM shell decreases monotonically with increasing volume fraction index. The largest and smallest critical loads are observed for homogeneous shells with aluminum and zirconia. The non-dimensional critical load remains constant beyond a particular thickness parameter (ξ_1) for long shells with low semi-vertex angles. The critical load decreases for increasing slenderness parameters (ξ_2) except for small semi-vertex angles and thickness parameters (ξ_1) greater than 0.1. In the latter case, the critical load drops initially, followed by an increasing trend before reducing again.

Appendix A

$$\mathbf{E} = \begin{bmatrix} \frac{\partial}{\partial s} & 0 & 0 & z \frac{\partial}{\partial s} & 0 \\ \frac{1}{s} & \frac{1}{s \sin \alpha} \frac{\partial}{\partial \theta} & \frac{1}{s \tan \alpha} & \frac{z}{s} & \frac{z}{s \sin \alpha} \frac{\partial}{\partial \theta} \\ \frac{1}{s \sin \alpha} \frac{\partial}{\partial \theta} & \frac{\partial}{\partial s} - \frac{1}{s} & 0 & \frac{z}{s \sin \alpha} \frac{\partial}{\partial \theta} & z \left(\frac{\partial}{\partial s} - \frac{1}{s} \right) \\ 0 & 0 & \frac{\partial}{\partial s} & 1 & 0 \\ 0 & -\frac{1}{s \tan \alpha} & \frac{1}{s \sin \alpha} \frac{\partial}{\partial \theta} & 0 & 1 \end{bmatrix} \quad (\text{A.1})$$

$$\mathbf{D} = \begin{bmatrix} \frac{E}{1-\nu^2} & \frac{\nu E}{1-\nu^2} & 0 & 0 & 0 \\ \frac{\nu E}{1-\nu^2} & \frac{E}{1-\nu^2} & 0 & 0 & 0 \\ 0 & 0 & \frac{E}{2(1+\nu)} & 0 & 0 \\ 0 & 0 & 0 & \frac{E}{2(1+\nu)} & 0 \\ 0 & 0 & 0 & 0 & \frac{E}{2(1+\nu)} \end{bmatrix} \quad (\text{A.2})$$

$$\begin{bmatrix} \gamma_1 \\ \gamma_2 \end{bmatrix} = \begin{bmatrix} \frac{1}{2\Omega_1} & \frac{\Omega_1}{2} \\ \frac{1}{2\Omega_2} & \frac{\Omega_2}{2} \end{bmatrix}^{-1} \begin{bmatrix} \zeta \\ \zeta \end{bmatrix} \quad (\text{A.3})$$

Appendix B

Numerical scheme for load jump algorithm to determine critical follower load

1. Define shell parameters r_2 , α , ξ_1 , ξ_2 , N_{elem} , boundary condition
2. Define material properties ν , E_i , E_r , ρ_i , ρ_r , η (for PFGM), ζ
3. Define required circumferential ($n \equiv 0 \dots n_{max}$) and longitudinal ($m \equiv 1 \dots m_{max}$) modes
4. Define minimum load increment parameter $\beta_{inc}^{min} = 10^{-4}$, maximum load increment parameter $\beta_{inc}^{max}(\zeta = 0) = 10^{-3}$, $\beta_{inc}^{max}(\zeta > 0) = 10^{-2}$, load accuracy parameter $\beta_{tol} = 10^{-6}$, load jump factor $j_\beta = 3$
5. For each n
 - a. Evaluate \mathbf{M} , \mathbf{K} and \mathbf{Q} matrices
 - b. If $\zeta > 0$
 - Compute first two natural frequencies from equation (14) keeping $\mathbf{Q} = \mathbf{0}$
 - Evaluate γ_1 , γ_2 and \mathbf{C} from equations (15) and (A.3)

- c. Initialize current load increment $\beta_{inc}^{cur} = \beta_{inc}^{min}$, load parameter $\beta = \beta_{inc}^{cur}$
- d. To identify critical load, while (true) do
 - i. Evaluate P from equation (20.5)
 - ii. If $\zeta = 0$
 - Obtain $\Lambda = \{\Lambda \mid \Lambda^2 \text{ is eigenvalue}\}$ from equation (14)
 - Else if $\zeta > 0$
 - Obtain $\Lambda = \{\Lambda \mid \Lambda \text{ is eigenvalue}\}$ from equation (17)
 - Redefine $\Lambda \equiv \Lambda - \{\Lambda \mid \text{Im}(\Lambda) < 0 \forall \Lambda \in \Lambda\}$
 - iii. Extract first m modes after sorting Λ by absolute magnitude
 - iv. Find the number of instability modes $NIM = |\{\Lambda \mid \text{Re}(\Lambda) > 0 \forall \Lambda \in \Lambda\}|$
 - v. If $NIM = 0$
 - Set $\beta_{prev} = \beta$
 - Set new increment $\beta_{inc}^{cur} = j_{\beta} \beta_{inc}^{cur}$
 - If $((\zeta = 0 \text{ and } \beta_{inc}^{cur} > \beta_{inc}^{max}(\zeta = 0)) \text{ or } (\zeta > 0 \text{ and } \beta_{inc}^{cur} > \beta_{inc}^{max}(\zeta > 0)))$, set $\beta_{inc}^{cur} = \beta_{inc}^{min}$
 - Set $\beta = \beta_{prev} + \beta_{inc}^{cur}$
 - Else if $(\zeta = 0 \text{ and } NIM > 2) \text{ or } (\zeta > 0 \text{ and } NIM > 1)$
 - Set $\beta_{inc}^{cur} = \beta_{inc}^{cur} / j_{\beta}$
 - Set $\beta = \beta_{prev} + \beta_{inc}^{cur}$
 - Else if $(\zeta = 0 \text{ and } (NIM = 1 \text{ or } NIM = 2)) \text{ or } (\zeta > 0 \text{ and } NIM = 1)$
 - Set $\beta_{range} = [\beta_{prev}, \beta]$
 - Exit while
- e. To improve accuracy, while $((\beta_{range}[2] - \beta_{range}[1]) > \beta_{tol})$ do
 - i. Compute $\beta = (\beta_{range}[2] + \beta_{range}[1]) / 2$
 - ii. Evaluate P from equation (20.5)
 - iii. If $\zeta = 0$
 - Obtain $\Lambda = \{\Lambda \mid \Lambda^2 \text{ is eigenvalue}\}$ from equation (14)
 - Else if $\zeta > 0$
 - Obtain $\Lambda = \{\Lambda \mid \Lambda \text{ is eigenvalue}\}$ from equation (17)
 - Redefine $\Lambda \equiv \Lambda - \{\Lambda \mid \text{Im}(\Lambda) < 0 \forall \Lambda \in \Lambda\}$
 - iv. Extract first m modes after sorting Λ by absolute magnitude
 - v. Find the number of instability modes $NIM = |\{\Lambda \mid \text{Re}(\Lambda) > 0 \forall \Lambda \in \Lambda\}|$
 - vi. If $NIM > 0$, set $\beta_{range}[2] = \beta$
 - Else set $\beta_{range}[1] = \beta$

- f. Set critical load for n^{th} mode $\beta_{cr}^{(n)} = (\beta_{range}[2] + \beta_{range}[1]) / 2$
- g. To check the type of instability
 - If $(\text{Re}(\Lambda) > 0 \text{ and } \text{Im}(\Lambda) \neq 0)$, the instability mode is flutter-type
 - Else if $(\text{Re}(\Lambda) > 0 \text{ and } \text{Im}(\Lambda) = 0)$, the instability mode is divergence-type
6. The least of all $\beta_{cr}^{(n)}$ for different n gives β_{cr}

Note: $|\cdot|$ denotes cardinality of the set

References

- Allahkarami, F., Ghassabzadeh Saryazdi, M. and Tohidi, H. 2020. Dynamic buckling analysis of bi-directional functionally graded porous truncated conical shell with different boundary conditions. *Composite Structures* 252, p. 112680. doi: 10.1016/j.compstruct.2020.112680.
- AminYazdi, A. 2021. Flutter of geometrical imperfect functionally graded carbon nanotubes doubly curved shells. *Thin-Walled Structures* 164, p. 107798. doi: 10.1016/j.tws.2021.107798.
- Avramov, K. and Uspensky, B. 2022. Nonlinear supersonic flutter of sandwich truncated conical shell with flexible honeycomb core manufactured by fused deposition modeling. *International Journal of Non-Linear Mechanics* 143, p. 104039. doi: 10.1016/j.ijnonlinmec.2022.104039.
- Avramov, K., Uspensky, B., Sakhno, N. and Nikonov, O. 2022. Transient response of functionally graded carbon nanotubes reinforced composite conical shell with ring-stiffener under the action of impact loads. *European Journal of Mechanics - A/Solids* 91, p. 104429. doi: 10.1016/j.euromechsol.2021.104429.
- Banijamali, S.M. and Jafari, A.A. 2023. Vibration analysis and critical speeds of a rotating functionally graded conical shell stiffened with Anisogrid lattice structure based on FSDT. *Thin-Walled Structures* 188, p. 110841. doi: 10.1016/j.tws.2023.110841.
- Barsoum, R.S. 1971. Finite element method applied to the problem of stability of a non-conservative system. *International Journal for Numerical Methods in Engineering* 3(1), pp. 63–87. doi: 10.1002/nme.1620030110.
- Bhangale, R.K., Ganesan, N. and Padmanabhan, C. 2006. Linear thermoelastic buckling and free vibration behavior of functionally graded truncated conical shells. *Journal of Sound and Vibration* 292(1–2), pp. 341–371. doi: 10.1016/J.JSV.2005.07.039.
- Chi, S. and Chung, Y.-L. 2003. Cracking in coating–substrate composites with multi-layered and FGM coatings. *Engineering Fracture Mechanics* 70(10), pp. 1227–1243. doi: 10.1016/S0013-7944(02)00114-5.
- Chi, S.H. and Chung, Y.L. 2006. Mechanical behavior of functionally graded material plates under transverse load—Part I: Analysis. *International Journal of Solids and Structures* 43(13), pp. 3657–3674. doi: 10.1016/J.IJSOLSTR.2005.04.011.

Chopra, A.K. 2012. *Dynamics of Structures: Theory and Applications to Earthquake Engineering*. Upper Saddle River, N.J.: Prentice Hall.

Fares, M.E., Elmarghany, M.Kh., Atta, D. and Salem, M.G. 2021. An improved layerwise formulation for free vibrations of multilayered FG truncated conical shells reinforced by carbon nanotubes. *Composite Structures* 275, p. 114372. doi: 10.1016/j.compstruct.2021.114372.

Flügge, W. 1966. *Stresses in shells*. New York: Springer-Verlag.

Fu, T., Wu, X., Xiao, Z. and Chen, Z. 2021. Study on dynamic instability characteristics of functionally graded material sandwich conical shells with arbitrary boundary conditions. *Mechanical Systems and Signal Processing* 151, p. 107438. doi: 10.1016/j.ymssp.2020.107438.

Hasan, H.M., Alkhfaji, S.S. and Mutlag, S.A. 2023. Torsional postbuckling characteristics of functionally graded graphene enhanced laminated truncated conical shell with temperature dependent material properties. *Theoretical and Applied Mechanics Letters* 13(4), p. 100453. doi: 10.1016/j.taml.2023.100453.

Houshang, A., Jafari, A.A., Haghighi, S.E. and Nezami, M. 2022. Supersonic flutter characteristics of truncated sandwich conical shells with MR core. *Thin-Walled Structures* 173, p. 108888. doi: 10.1016/j.tws.2022.108888.

Huang, X., Wang, J., Wei, N., Wang, C. and Ma, B. 2023. Buckling and vibration of porous sigmoid functionally graded conical shells. *Journal of Theoretical and Applied Mechanics* 61(3), pp. 559–571. doi: 10.15632/jtam-pl/168072.

Ibrahim, H.H., Tawfik, M. and Al-Ajmi, M. 2008. Non-linear panel flutter for temperature-dependent functionally graded material panels. *Computational Mechanics* 41(2), pp. 325–334. doi: 10.1007/s00466-007-0188-4.

Ibrahim, H.H., Yoo, H.H. and Lee, K.-S. 2009. Supersonic Flutter of Functionally Graded Panels Subject to Acoustic and Thermal Loads. *Journal of Aircraft* 46(2), pp. 593–600. doi: 10.2514/1.39085.

Irie, T., Yamada, G. and Tanaka, K. 1984. Natural frequencies of truncated conical shells. *Journal of Sound and Vibration* 92(3), pp. 447–453. doi: 10.1016/0022-460X(84)90391-2.

Jung, W.Y. and Han, S.C. 2014. Transient analysis of FGM and laminated composite structures using a refined 8-node ANS shell element. *Composites Part B: Engineering* 56, pp. 372–383. doi: 10.1016/J.COMPOSITESB.2013.08.044.

Kayran, A. and Vinson, J.R. 1990. Free vibration analysis of laminated composite truncated circular conical shells. *AIAA Journal* 28(7), pp. 1259–1269. doi: 10.2514/3.25203.

Kim, J.H. and Kim, H.S. 2000. A study on the dynamic stability of plates under a follower force. *Computers & Structures* 74(3), pp. 351–363. doi: 10.1016/S0045-7949(99)00023-1.

Koizumi, M. 1997. FGM activities in Japan. *Composites Part B: Engineering* 28(1–2), pp. 1–4. doi: 10.1016/S1359-8368(96)00016-9.

- Koizumi, M. and Niino, M. 1995. Overview of FGM Research in Japan. *MRS Bulletin* 20(1), pp. 19–21. doi: 10.1557/S0883769400048867.
- Langthjem, M.A. and Sugiyama, Y. 2000. Dynamic stability of columns subjected to follower loads: A survey. *Journal of Sound and Vibration* 238(5), pp. 809–851. doi: 10.1006/JSVI.2000.3137.
- Leissa, A.W. 1993. *Vibration of Shells*. Washington, D.C.: Acoustical Society of America.
- Li, H., Hao, Y.X., Zhang, W., Liu, L.T., Yang, S.W. and Wang, D.M. 2021. Vibration analysis of porous metal foam truncated conical shells with general boundary conditions using GDQ. *Composite Structures* 269, p. 114036. doi: 10.1016/j.compstruct.2021.114036.
- Liew, K.M., Ng, T.Y. and Zhao, X. 2005. Free vibration analysis of conical shells via the element-free kp-Ritz method. *Journal of Sound and Vibration* 281(3–5), pp. 627–645. doi: 10.1016/J.JSV.2004.01.005.
- Mahmoudkhani, S., Haddadpour, H. and Navazi, H.M. 2010. Supersonic flutter prediction of functionally graded conical shells. *Composite Structures* 92(2), pp. 377–386. doi: 10.1016/J.COMPSTRUCT.2009.08.018.
- Malekzadeh, P., Fiouz, A.R. and Sobhrouyan, M. 2012. Three-dimensional free vibration of functionally graded truncated conical shells subjected to thermal environment. *International Journal of Pressure Vessels and Piping* 89, pp. 210–221. doi: 10.1016/J.IJPVP.2011.11.005.
- Muc, A. and Flis, J. 2021. Flutter characteristics and free vibrations of rectangular functionally graded porous plates. *Composite Structures* 261, p. 113301. doi: 10.1016/J.COMPSTRUCT.2020.113301.
- Nejati, M., Asanjarani, A., Dimitri, R. and Tornabene, F. 2017. Static and free vibration analysis of functionally graded conical shells reinforced by carbon nanotubes. *International Journal of Mechanical Sciences* 130, pp. 383–398. doi: 10.1016/j.ijmecsci.2017.06.024.
- Novozhilov, V.V. 1964. *Thin shell theory*. Groningen: P. Noordhoff.
- Park, S.H. and Kim, J.H. 2000. Dynamic stability of a completely free circular cylindrical shell subjected to a follower force. *Journal of Sound and Vibration* 231(4), pp. 989–1005. doi: 10.1006/JSVI.1999.2319.
- Reddy, J.N. 2000. Analysis of functionally graded plates. *International Journal for Numerical Methods in Engineering* 47(1–3), pp. 663–684. doi: 10.1002/(SICI)1097-0207(20000110/30)47:1/3<663::AID-NME787>3.0.CO;2-8.
- Sabri, F. and Lakis, A.A. 2013. Efficient Hybrid Finite Element Method for Flutter Prediction of Functionally Graded Cylindrical Shells. *Journal of Vibration and Acoustics* 136(1). Available at: <https://doi.org/10.1115/1.4025397>.
- Sanders, J.L. 1959. *An improved first-approximation theory for thin shells*. Washington, D.C.: NASA.
- Shu, C. 1996. An efficient approach for free vibration analysis of conical shells. *International Journal of Mechanical Sciences* 38(8–9), pp. 935–949. doi: 10.1016/0020-7403(95)00096-8.

Simites, G. and Hodges, D.H. 2006. *Fundamentals of Structural Stability*. Burlington, USA: Butterworth-Heinemann Publications, Elsevier.

Soedel, W. 2004. *Vibrations of Shells and Plates*. 3rd ed. Boca Raton: CRC Press.

Sofiyev, A.H. 2012. The non-linear vibration of FGM truncated conical shells. *Composite Structures* 94(7), pp. 2237–2245. doi: 10.1016/J.COMPSTRUCT.2012.02.005.

Song, Z., Cao, Q. and Dai, Q. 2019. Free vibration of truncated conical shells with elastic boundary constraints and added mass. *International Journal of Mechanical Sciences* 155, pp. 286–294. doi: 10.1016/j.ijmecsci.2019.02.039.

Su, Z., Wang, L., Sun, K. and Wang, D. 2019. Vibration characteristic and flutter analysis of elastically restrained stiffened functionally graded plates in thermal environment. *International Journal of Mechanical Sciences* 157–158, pp. 872–884. doi: 10.1016/J.IJMECSCI.2019.05.028.

Sun, Y., Song, Z., Ma, W. and Li, F. 2021. Influence mechanism of lumped masses on the flutter behavior of structures. *Aerospace Science and Technology* 111, p. 106524. doi: 10.1016/J.AST.2021.106524.

Tong, L. 1993. Free vibration of composite laminated conical shells. *International Journal of Mechanical Sciences* 35(1), pp. 47–61. doi: 10.1016/0020-7403(93)90064-2.

Torki, M.E., Kazemi, M.T., Haddadpour, H. and Mahmoudkhani, S. 2014a. Dynamic stability of cantilevered functionally graded cylindrical shells under axial follower forces. *Thin-Walled Structures* 79, pp. 138–146. doi: 10.1016/J.TWS.2013.12.005.

Torki, M.E., Kazemi, M.T., Reddy, J.N., Haddadpoud, H. and Mahmoudkhani, S. 2014b. Dynamic stability of functionally graded cantilever cylindrical shells under distributed axial follower forces. *Journal of Sound and Vibration* 333(3), pp. 801–817. doi: 10.1016/J.JSV.2013.09.005.

Tornabene, F., Viola, E. and Inman, D.J. 2009. 2-D differential quadrature solution for vibration analysis of functionally graded conical, cylindrical shell and annular plate structures. *Journal of Sound and Vibration* 328(3), pp. 259–290. doi: 10.1016/J.JSV.2009.07.031.

Trabelsi, S., Frikha, A., Zghal, S. and Dammak, F. 2018. Thermal post-buckling analysis of functionally graded material structures using a modified FSDT. *International Journal of Mechanical Sciences* 144, pp. 74–89. doi: 10.1016/j.ijmecsci.2018.05.033.

Trabelsi, S., Frikha, A., Zghal, S. and Dammak, F. 2019. A modified FSDT-based four nodes finite shell element for thermal buckling analysis of functionally graded plates and cylindrical shells. *Engineering Structures* 178, pp. 444–459. doi: 10.1016/j.engstruct.2018.10.047.

Trabelsi, S., Zghal, S. and Dammak, F. 2020. Thermo-elastic buckling and post-buckling analysis of functionally graded thin plate and shell structures. *Journal of the Brazilian Society of Mechanical Sciences and Engineering* 42(5), p. 233. doi: 10.1007/s40430-020-02314-5.

Vescovini, R. and Fantuzzi, N. 2023. Free vibrations of conical shells via Ritz method. *International Journal of Mechanical Sciences* 241, p. 107925. doi: 10.1016/j.ijmecsci.2022.107925.

Vlasov, V.Z. 1964. *General theory of shells and its applications in engineering*. Washington, D.C.: NASA.

Wang, J., Wang, Y.Q. and Chai, Q. 2022. Free vibration analysis of a spinning functionally graded spherical–cylindrical–conical shell with general boundary conditions in a thermal environment. *Thin-Walled Structures* 180, p. 109768. doi: 10.1016/j.tws.2022.109768.

Wei, J., Song, Z. and Li, F. 2020. Superior aeroelastic behaviors of axially functional graded cylindrical shells in supersonic airflow. *Journal of Fluids and Structures* 96, p. 103027. doi: 10.1016/J.JFLUIDSTRUCTS.2020.103027.

Zarei, M., Rahimi, G.H. and Hemmatnezhad, M. 2020. Global buckling analysis of laminated sandwich conical shells with reinforced lattice cores based on the first-order shear deformation theory. *International Journal of Mechanical Sciences* 187, p. 105872. doi: 10.1016/j.ijmecsci.2020.105872.

Zghal, S. and Dammak, F. 2021. Vibration characteristics of plates and shells with functionally graded pores imperfections using an enhanced finite shell element. *Computers & Mathematics with Applications* 99, pp. 52–72. doi: 10.1016/j.camwa.2021.08.001.

Zghal, S., Frikha, A. and Dammak, F. 2018a. Free vibration analysis of carbon nanotube-reinforced functionally graded composite shell structures. *Applied Mathematical Modelling* 53, pp. 132–155. doi: 10.1016/j.apm.2017.08.021.

Zghal, S., Frikha, A. and Dammak, F. 2018b. Mechanical buckling analysis of functionally graded power-based and carbon nanotubes-reinforced composite plates and curved panels. *Composites Part B: Engineering* 150, pp. 165–183. doi: 10.1016/j.compositesb.2018.05.037.

Zghal, S., Trabelsi, S. and Dammak, F. 2022. Post-buckling behavior of functionally graded and carbon-nanotubes based structures with different mechanical loadings. *Mechanics Based Design of Structures and Machines* 50(9), pp. 2997–3039. doi: 10.1080/15397734.2020.1790387.

Zghal, S., Trabelsi, S., Frikha, A. and Dammak, F. 2021. Thermal free vibration analysis of functionally graded plates and panels with an improved finite shell element. *Journal of Thermal Stresses* 44(3), pp. 315–341. doi: 10.1080/01495739.2021.1871577.

Zhao, X. and Liew, K.M. 2011. Free vibration analysis of functionally graded conical shell panels by a meshless method. *Composite Structures* 93(2), pp. 649–664. doi: 10.1016/J.COMPSTRUCT.2010.08.014.

Zhou, X., Wang, Y. and Zhang, W. 2021. Vibration and flutter characteristics of GPL-reinforced functionally graded porous cylindrical panels subjected to supersonic flow. *Acta Astronautica* 183, pp. 89–100. doi: 10.1016/J.ACTAASTRO.2021.03.003.